Materials Science & Engineering C 88 (2018) 32–45

Contents lists available at ScienceDirect

Materials Science & Engineering C

journal homepage: www.elsevier.com/locate/msec

Enhanced cellular uptake of LHRH-conjugated PEG-coated magnetite nanoparticles for specific targeting of triple negative breast cancer cells

J. Hu[a,b], J.D. Obayemi[a,b,c], K. Malatesta[a,b], A. Košmrlj[a,b], W.O. Soboyejo[a,b,c,d,*]

[a] Department of Mechanical and Aerospace Engineering, Princeton University, Olden Street, Princeton, NJ 08544, USA
[b] Princeton Institute of Science and Technology of Materials (PRISM), Princeton University, 70 Prospect Street, Princeton, NJ 08544, USA
[c] Department of Mechanical Engineering, Higgins Lab, 100 Institute Road, Worcester Polytechnic Institute (WPI), Worcester, MA 01609, USA
[d] Department of Biomedical Engineering, Gateway Park Life Sciences Center, 60 Prescott Street, Worcester Polytechnic Institute (WPI), Worcester, MA 01605, USA

ARTICLE INFO

Keywords:
Luteinizing hormone releasing hormone (LHRH)
LHRH-conjugated PEG-coated magnetite nanoparticles (LHRH-MNPs)
Triple negative breast cancer (TNBC)
Specific targeting

ABSTRACT

Targeted therapy is an emerging technique in cancer detection and treatment. This paper presents the results of a combined experimental and theoretical study of the specific targeting and entry of luteinizing hormone releasing hormone (LHRH)-conjugated PEG-coated magnetite nanoparticles into triple negative breast cancer (TNBC) cells and normal breast cells. The conjugated nanoparticles structures, cellular uptake of PEG-coated magnetite nanoparticles (MNPs) and LHRH-conjugated PEG-coated magnetite nanoparticles (LHRH-MNPs) into breast cancer cells and normal breast cells were investigated using a combination of transmission electron microscope, optical and confocal fluorescence microscopy techniques. The results show that the presence of LHRH enhances the uptake of LHRH-MNPs into TNBC cells. Nanoparticle entry into breast cancer cells is also studied using a combination of thermodynamics and kinetics models. The trends in the predicted nanoparticle entry times (into TNBC cells) and the size ranges of the engulfed nanoparticles (within the TNBC cells) are shown to be consistent with experimental observations. The implications of the results are then discussed for the specific targeting of TNBCs with LHRH-conjugated PEG-coated magnetite nanoparticles for the early detection and treatment of TNBC.

1. Introduction

Breast cancer is one of the most commonly diagnosed carcinoma in women throughout the world, and in 2016 it has emerged as the leading cause of cancer deaths in women in the U.S. that are between 20 and 59 years old [1]. Among the subtypes of breast carcinoma, triple negative breast cancer (TNBC) has poorer prognosis and clinical outcomes compared to other types of breast cancer [2,3]. It accounts for approximately 15% of all breast cancers [4], but is associated with unproportionally high recurrence and mortality rates [5]. TNBC is estrogen-receptor (ER) negative, progesterone-receptor (PR) negative and also HER2 negative [2,3]. Hence, it is not responsive to established therapies that are often designed to target those receptors, e.g. hormone therapies (ER or PR positive) and anti-HER2 targeted therapy (HER2 positive) [2]. Instead, TNBC is usually treated with a combination radiation therapy and chemotherapy [6]. These two commonly used breast cancer adjuvant therapies are non-targeted pathways, which lead to both severe short-term and long-term side effects [7–9]. These facts clearly indicate the need for new TBNC treatment techniques to improve the clinical outcomes.

Nanotechnology provides a revolutionary platform for cancer therapy [10,11] and biomedical application [12,13]. Extensive studies have been conducted in this fertile area to create theranostic nanocarriers, which can be inorganic (e.g. metal nanostructure [14–17], metal-oxide nanoparticles [18–20]), organic (e.g. carbon dots [21,22], liposomes [23,24]) or hybrid (two or more constituents [10,25,26]). Within this context, magnetite nanoparticles have attracted significant attention in recent years. This is due to their potential applications in cancer detection and treatment. These include: hyperthermia [27–29]; magnetic resonance imaging [30–32]; drug targeting [33–35] and gene transfer [36–38].

To date, it is still challenging to design tumor-specific targets for TNBC. Luteinizing Hormone-Releasing Hormone (LHRH) [39,40] is one of the specific targeting receptors for TNBC cells, as over 50% of human TNBC cells express binding sites (receptors) for LHRH [39,41,42]. Efforts have been made to investigate LHRH expression on TNBC cells, including inhibitors studies [39], as well as the studies of LHRH receptor binding affinity and capacity [43]. The results have shown that LHRH ligands bind specifically to LHRH receptors, indicating that the interactions between the over-expressed LHRH receptors and LHRH

* Corresponding author at: Atwater Kent 128, 100 Institute Road, Worcester, MA 01609, USA.
E-mail addresses: soboyejo@princeton.edu, wsoboyejo@wpi.edu (W.O. Soboyejo).

https://doi.org/10.1016/j.msec.2018.02.017
Received 3 July 2017; Received in revised form 26 August 2017; Accepted 20 February 2018

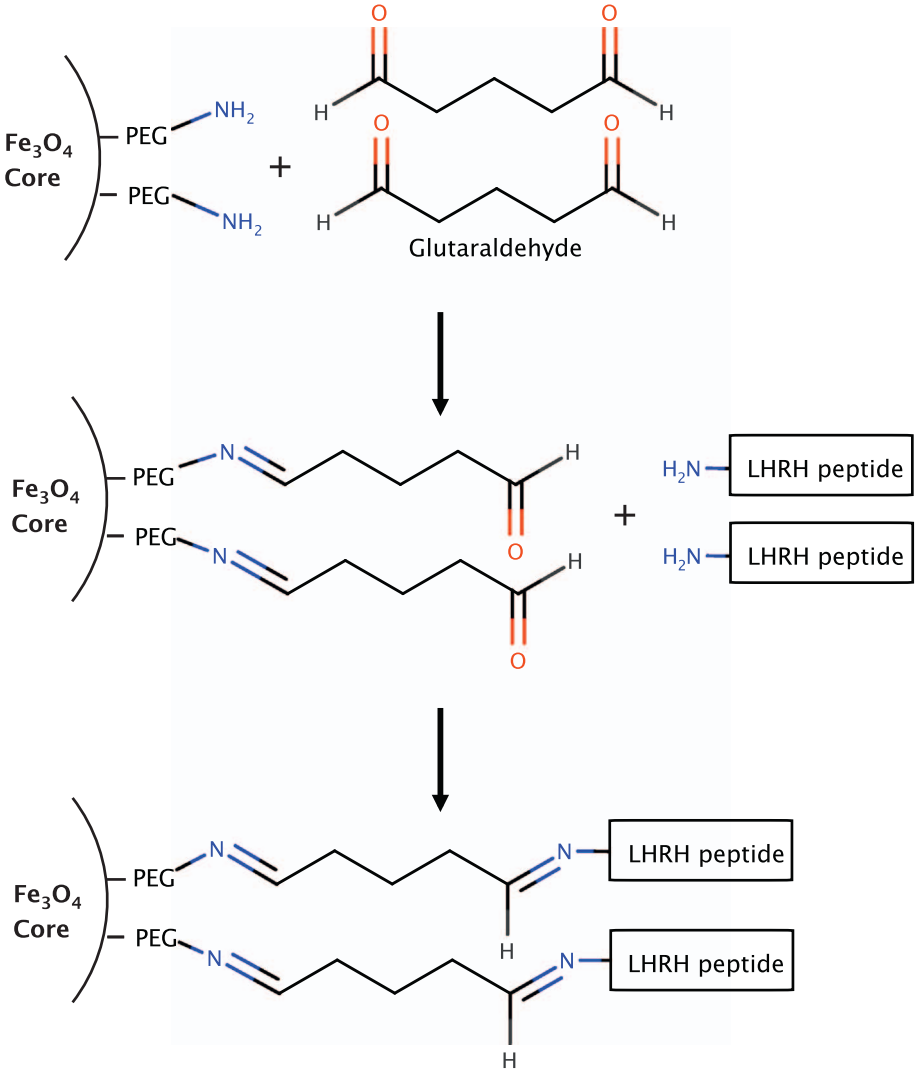

Fig. 1. Schematic of nanoparticle conjugation process.

ligands enable the specific targeting of breast cancer cells [30,44]. Prior studies [30,43,45] used carbodiimide cross-linking chemistry to attach LHRH ligands to the surfaces of bare magnetite nanoparticles. These molecular recognition units facilitated the specific delivery of magnetite nanoparticles, which enhanced the MRI signals of breast tumor sites and their metastases in the body [30,46].

However, a major drawback of magnetite nanoparticles with bare surfaces is that they tend to aggregate, due to their high surface energies, and become unstable [47–50]. Furthermore, the results from prior studies [30] suggest that LHRH-conjugated bare magnetite nanoparticles tends to aggregate further after carbodiimide reaction. This may be due to the lack of protection of carboxylic acid on the LHRH peptide, resulting peptide cross-linking to itself [51]. Consequently, the oversized magnetite nanoparticle clusters will be readily detected and eliminated by macrophage cells as part of the body's immune system. This results in reduced efficacy of nanoparticle delivery and decreased cellular uptake of magnetite nanoparticles into targeting cells [52–55]. Lastly, the dissolution of surface Fe could potentially result in high local concentrations of Fe ions that can induce possible toxicity effects in biological organisms [56,57].

To circumvent the above-mentioned challenges, the addition of polymer surface coatings to nanoparticle cores offers great opportunities for the tuning of the physiochemical properties of nanocarriers [58–61]. In current work, magnetite nanoparticles with polyethylene glycol (PEG) coatings are explored. PEG has been shown to improve both hydrophilicity and biocompatibility of magnetite nanoparticles [62,63]. PEG-coated magnetite nanoparticles are also well stabilized in cell culture media, with negligible aggregation [64–67]. Thus, the non-specific uptake of PEG-coated magnetite nanoparticles (by macrophage cells) has been found to be reduced significantly [65–69]. In addition, we use an alternative conjugation process to link LHRH peptides onto the surfaces of PEG-coated magnetite nanoparticles (MNPs). The new nanocarrier is shown to exhibit improved monodispersity and stability.

In the present study, the entry and cellular uptake of this new nanocarrier, LHRH-conjugated PEG-coated magnetite nanoparticles (LHRH-MNPs), into TNBC cells is investigated using experimental and theoretical approaches. First, we introduce MNPs and LHRH-MNPs into normal/cancerous breast cells, respectively. The cellular uptake of MNPs and LHRH-MNPs is then elucidated using a combination of optical and confocal fluorescence microscopy. The cluster size distributions at different incubation times are used to evaluate cellular uptake. Next, we adapt and extend prior mathematical models [30,70] to the study of the kinetics of nanocluster entry into normal breast cells and breast cancer cells. This is used to illustrate the delivery efficacy of the LHRH-MNPs into breast cancer cells. Lastly, the predictions from the models are compared with experimental results. The trends in predicted nanoparticle entry times and the size ranges of the engulfed nanoparticles are shown to be in good agreement with experimental

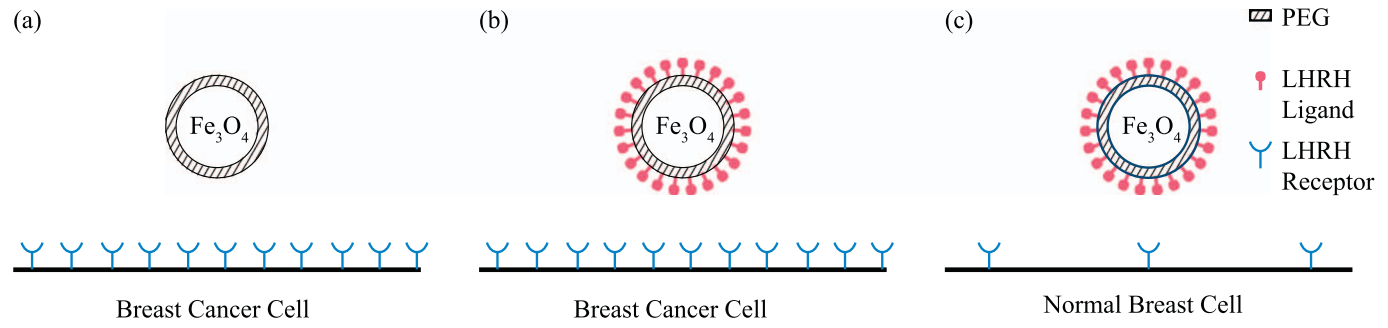

Fig. 2. Schematic of different nanoparticle/cell interactions: (a) MNPs/MDA-MB-231 breast cancer cells; (b) LHRH-MNPs/MDA-MB-231 breast cancer cells; and (c) LHRH-MNPs/MCF-10A normal breast cells.

observations. The implications of the results are discussed for potential applications of LHRH-conjugated PEG-coated magnetite nanoparticles in the specific targeting of triple negative breast cancer cells.

2. Materials and methods

2.1. Materials

PEG-coated magnetite nanoparticles (MNPs) were purchased in solution from Ocean NanoTech (Cat # SHA30, San Diego, CA, USA). (D-Trp^6)-LHRH was purchased from Bachem Americas (Torrance, CA, USA). The surfaces of these particles were functionalized with amine groups to enable further conjugation of the nanoparticle. The LHRH analog has an amino acid sequence of Pyr-His-Trp-Ser-Tyr-D-Trp-Leu-Arg-Pro-Gly-NH_2 (Cat # H-4005-GMP). Glutaraldehyede (Grade II, Cat # G5257) and bovine serum albumin (BSA) (Cat # A2058) were purchased from Sigma-Aldrich (St. Louis, MO, USA). TEM grids (Cat # CF300-Cu), 1× phosphate buffered saline (PBS, Cat # 19344) and paraformaldehyde (4% in 0.1 M phosphate buffered saline, Cat # 157-4) were all obtained from Electron Microscopy Science (Hatfield, PA). Spin columns (MWCO 100 kDa) were obtained from Pall Corporation (Port Washington, NY). Coverslips (No.1.5 thickness, Cat # PCS-1.5) were purchased from MatTek Corporation (Ashland, MA, USA). The MDA-MB-231 (Cat # HTB-26) cell line was purchased from American Type Culture Collection (ATCC, Manassas, VA, USA). The MCF-10A, normal breast cell line was provided by Prof. Yibin Kang of Princeton University, USA. Triton X-100 was obtained from Life Technologies Corporation (Carlsbad, CA, USA, Cat. # HFH10). Anti-LHRH antibody was purchased from EMD Millipore (Darmstadt, Germany, Cat # AB-1567). Anti-mouse IgG conjugated with Alexa fluor 488 (Cat. # 32723) was bought from Thermo Fisher Scientific, Inc. (Waltham, MA, USA). FluoroGuard Antifade Reagent (Cat # 1703140) was purchased from Bio-Rad Laboratories (Hercules, CA, USA).

2.2. Conjugation of LHRH peptide to MNPs

Luteinizing hormone releasing hormone (LHRH) peptide was conjugated to PEG-coated magnetite nanoparticles through glutaraldehyde cross-linking chemistry [71,72]. The reaction process is illustrated in Fig. 1. Specifically, 0.5 mL of deionized (DI) water was added to 0.25 mL of 1 mg Fe/mL of MNP aqueous solution, as originally received. 50 μL glutaraldehyde was then added into the diluted MNP solution and the mixture was left overnight to react at room-temperature (25 °C). The resulting solution was purified three times with DI water using a spin column with a membrane pore size of 100 kDa. This was done to remove excess glutaraldehyde. The purified particles were then re-suspended in 0.3 mL of deionized (DI) water. Subsequently, 0.1 mL of LHRH solution (0.1 mg/mL in DI water) was then added to the resulting glutaraldehyde-activated MNP solution, before leaving the mixture overnight at 4 °C under conditions of continuous mixing. Unreacted LHRH was removed from the suspension using a spin column with a molecular weight cutoff of 50 kDa. The particles were then re-suspended in 0.2 mL of DI water and stored at 4 °C in a new vial.

2.3. Characterization of nanoparticles

TEM samples of the resulting LHRH-conjugated MNPs were studied using a Philips CM100 Transmission Electron Microscope (TEM) (Philips, Amsterdam, Netherlands). High-resolution TEM images and EDS spectra were obtained from a Philips CM200 FEG-TEM (Philips, Amsterdam, Netherlands). Iron oxide phase identification was carried out in a Raman Spectrometer (Horiba Scientific, Kyoto, Japan) with a 630 nm wavelength laser. The hydrodynamic size and polydispersity index (PDI) of nanoparticles was obtained using dynamic light scattering (DLS) in a Zetasizer Nano ZS particle size analyzer (Malvern Instruments, Malvern, United Kingdom). Zeta potential measurements were performed by diluting the nanoparticle suspension with 10 mM NaCl solution using the same particle size analyzer. The surface chemistry of the nanoparticles was characterized using Fourier Transform Infrared Spectroscopy (FTIR). FTIR spectra were acquired using an IRAffinity-1S spectrometer (Shimadzu, Kyoto, Japan). The core diameters of nanoparticles were quantified by analyzing TEM micrographs with the ImageJ software package (ImageJ software, NIH, Bethesda, MD, USA).

2.4. Nanoparticle internalization

The following three nanoparticle/cell pairs were used to study the internalization of the nanoparticles: MNPs with MDA-MB-231 breast cancer cells; LHRH-MNPs with MDA-MB-231 breast cancer cells, and LHRH-MNPs with MCF-10A normal breast cells (Fig. 2). The cells were cultured in their respective media on No. 1.5 sterile coverslips as described in Ref. [73]. They were then incubated with the different types of particles (100 μL) at a concentration of 0.2 mg Fe/mL. This was done for durations of 5 min, 30 min, 1 h and 3 h.

After incubation, the cell culture medium was removed and the cell samples were washed thrice with PBS. The cells were then fixed with 4 wt% paraformaldehyde solution for 10 min at room-temperature (25 °C). The samples were then rinsed three more times in PBS solution, before a final rinse with purified water. The resulting samples (on the coverslips) were drained and mounted on clean glass slides, with a small drop of FluoroGuard Reagent as the mounting medium and nail polish as a sealant.

The cells with the incubated nanoparticles were imaged using a Nikon total internal reflection fluorescence (TIRF) microscope (Nikon Instruments Inc., Melville, New York, USA) with a 20× air objective and a 60× oil-immersion objective.

2.5. Internalized cluster size distribution and uptake characterization

To evaluate uptake cluster size distribution, five samples were examined using TIRF microscopy. Due to contrast difference and

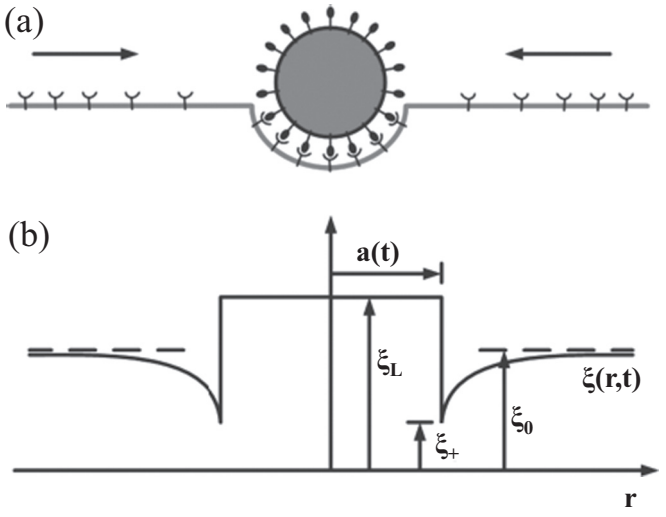

Fig. 3. Schematics of (a) contact on an initially flat membrane containing diffusive receptor molecules wrapping around a ligand-coated particle; and (b) receptor density distribution on membrane surfaces
(Adapted and modified from [70].)

clustering during nanoparticles uptake, the changes during the process were able to be monitored using TIRF. This was used to study the uptake of nanoparticles into cells that were attached to coverslip substrates. Within each sample, six locations were randomly selected with a total of over 300 cells being imaged. The diameters of detectable clusters were measured using ImageJ software package (ImageJ software, NIH, Bethesda, MD, USA).

The uptake efficiency of nanoparticles into cells was estimated by taking the ratio of the total area of observable clusters that are fully engulfed to the total area of cells in the imaging field.

2.6. Immunofluorescence staining of LHRH receptors

In this study, the immunofluorescence staining of the triple negative breast cancer cells (MDA-MB-231) was used to study the distributions of LHRH receptors for the specific attachment of conjugated MNPs. 2×10^4 MDA-MB-231 cells were cultured on No. 1.5 coverslips inside of a sterile 60 × 15 mm Falcon cell culture Petri dish in their medium. After at least 48 h, the cells were fixed with 4% high-grade paraformaldehyde in 0.1 M Phosphate Buffered Saline (PBS) solution. After 10 min, the paraformaldehyde was aspirated. This was followed by three rinses with PBS. The cell samples were then permeabilized, each with 1 mL 0.1% solution of Triton X-100 for 5 min. This was followed by three rinses with PBS. Subsequently, the cell samples were incubated in PBS with 3% bovine serum albumin (BSA) at room temperature (25 °C) for 15 min. The samples were then rinsed thrice with PBS, before incubating the cells for 2 h with 100 μL of primary antibody (anti-LHRH antibody) at a concentration of 5 μg/mL. This was followed by three rinses with PBS to remove excess anti-LHRH antibody.

The cells were then incubated with 100 μL of secondary antibody (anti-mouse IgG conjugated with Alexa fluor 488) prepared at a concentration of 10 μg/mL in 1% BSA solution for 1 h. The resulting cell samples were then rinsed three times with 2 mL of PBS. Finally, the cell nuclei were stained with 5 μg/mL of DAPI for 10 min, followed by three rinses with PBS. The resulting samples (on the coverslips) were drained and mounted on clean glass slides, with a small drop of FluoroGuard Reagent added as the mounting medium.

The staining was carried out to reveal the interactions of LHRH-MNPs with MDA-MB-231 breast cancer cells after 1-h and also after 3-h of incubation. This was done to verify the internalization of the particles. The stained and fixed cell samples were imaged using an oil-immersion objective (60×) in a Nikon A1RSi laser scanning confocal microscope (Nikon Instruments Inc., Melville, New York, USA). Five samples (per condition) were examined under the confocal microscope. This was used to study nanoparticle entry at six locations that were selected on cells that were attached to coverslip substrates.

2.7. Statistical analysis

The raw data were analyzed using one-way ANOVA. Statistical difference between the means were considered significant at $p < 0.05$.

3. Theory

3.1. Single particle entry model

Receptor-ligand interactions enable nanoparticles to enter into biological cells by receptor-mediated endocytosis [74,75]. This is one of the most important processes by which viruses, digested food particles and ligand-conjugated nanoparticles enter into biological cells [70,74,76]. To understand the possible factors that can affect receptor-mediated endocytosis, Gao et al. [70] have used thermodynamics and kinetics concepts to study the interactions between a ligand coated nanoparticle and receptors that are present on the cell membrane. In their model, since the 2D membrane is assumed to have circular symmetry, the problem is reduced to receptors moving along a semi-infinite 1D line.

Before contact of nanoparticle, the receptors are uniformly distributed along the cell membrane with a density of ξ_0. The receptors can move along the cell membrane via rapid diffusion motion, while the ligands are considered to be immobile on the surface of the nanoparticles, with a density of ξ_L. Since the nanoparticle size is significantly smaller than the cell membrane size, which is on the order of 10 μm, the cell membrane is considered to be a flat sheet before contact occurs [70] (Fig. 3). The distance from the origin of the nanoparticle is denoted as r, with the receptor density being described as $\xi(r,t)$ along the cell membrane at different time, t (Fig. 3). ξ_+ represents the receptor density directly at the contact front. The diffusivity of membrane receptors is denoted as D.

During the engulfment of nanoparticle, membrane receptors bind to ligands on nanoparticle in order to reduce the free energy of the system. Hence, the local receptor density is raised to the level of the ligand density, ξ_L, which leads to a depletion of the receptor density in the vicinity of nanoparticle. The resulting gradient of receptor densities near the nanoparticle drives the flux of receptors towards the nanoparticle (Fig. 3). The receptor-ligand interactions cause the cell membrane to bend and wrap around the nanoparticle at a cost of elevated elastic energy [70]. During the engulfment, Gao et al. [70] consider the following three contributions to the free energy change: the receptor-ligand binding; the cell membrane bending energy; and the entropy for both ligand-bound and free receptors. Therefore, the overall free energy change associated with the engulfment of the nanoparticle via receptor-mediated endocytosis is given by:

$$F(t) = 2\pi k_B T \left\{ \int_0^{a(t)} \left(-\xi_L e_{RL} + \xi_L \ln \frac{\xi_L}{\xi_0} + \frac{1}{2} B \kappa_p^2 \right) r dr + \int_{a(t)}^{L} \left(\xi \ln \frac{\xi}{\xi_0} \right) r dr \right\} \quad (1)$$

where k_B is the Boltzmann constant, T is the absolute temperature, $a(t)$ is the radius of the contact region, $k_B T e_{RL}$ is the binding energy per receptor-ligand bond, B is the bending modulus (in units of $k_B T$), and κ_p is the total mean curvature. For spherical particles with radius R, $\kappa_p = 1/R_1 + 1/R_2 = 2/R$. Terms $k_B T \ln(\xi_L/\xi_0)$ and $k_B T \ln(\xi/\xi_0)$ correspond to the free energy per receptor associated with the change in configurational entropy of the bound and free receptors, respectively. The bending energy per unit area for wrapping of the cell membrane

around a sphere is given by $1/2k_BTB{\kappa_p}^2$. Eq. (1) is slightly modified from the results presented in Ref. [70] to address the spherical symmetry of particle.

3.2. Nanoparticle cluster entry model

Experimental studies have shown that nanoparticles can also enter cells as nanoparticle clusters [30]. Since the formation of clusters is associated with changes in the surface energies, a new model is presented here to account for the extra surface energy terms associated with nanoparticle clusters. Meng et al. [30] proposed that the additional new surface energy terms include interactions between nanoparticles, surface energy between the nanoparticle and the cell culture medium and the interfacial energy between the nanoparticles and the cell membrane. The clusters are assumed to be face centered closed packed, as each particle on the surface has six nearest neighbors, while the ones in the middle have twelve. Hence, the additional surface energy terms are given by [30]:

$$U_{surface\ enery} = U_{MNP-MNP} + U_{MNP-medium} + U_{MNP-cell\ membrane} \tag{2}$$

With the new surface energy term and considering only the time dependent term, the new free energy equation is obtained by modifying the results of Meng et al. [30] to give:

$$F(t) = 2\pi k_B T\left\{\int_0^{a(t)}\left(-\xi_L e_{RL} + \xi_L ln\frac{\xi_L}{\xi_0} + \frac{1}{2}B\kappa_p^2 - \frac{\gamma_1-\gamma_2}{k_BT}\right)rdr + \int_{a(t)}^{L}\left(\xi ln\frac{\xi}{\xi_0}\right)rdr\right\} \tag{3}$$

where γ_1 represents the surface energy between the nanoparticle-cell culture medium and body fluids, and γ_2 is the surface energy between a nanoparticle cluster and the cell membrane. Note that the interactions between nanoparticles contribute additional constant terms in the free energy, which do not affect the kinetics of receptors and have thus been omitted [30]. Eq. (3) above suggests that the inclusion of the new energy term can be interpreted as an effective change in the interaction energy between receptor-ligand pairs. Note that κ_p is now related to the total mean curvature of the whole cluster.

Balance of chemical potentials of receptors inside the contact region and of receptors immediately outside the contact region leads to the following equation:

$$-e_{RL} + ln\frac{\xi_L}{\xi_0} + \frac{B\kappa_p^2}{2\xi_L} - \frac{\gamma_1-\gamma_2}{\xi_L k_B T} = ln\frac{\xi_+}{\xi_0}, \tag{4}$$

Eq. (4) can be used to determine the density of receptors ξ_+ immediately outside the contact region. This gives:

$$\xi_+ = \xi_L \exp\left[-e_{RL} + \frac{B}{2\xi_L}\left(\frac{2}{R}\right)^2 - \frac{\gamma_1-\gamma_2}{\xi_L k_B T}\right]. \tag{5}$$

The entry of nanoparticle clusters is thermodynamically favorable when the chemical potential of receptors (bound to the ligand) is smaller than the chemical potential of free receptors in the membrane, or equivalently when $\xi_+ < \xi_0$. This condition requires that the radius of clusters satisfies the following inequality:

$$R_{min} > \sqrt{\frac{2B}{\xi_L\left(e_{RL} + \frac{\gamma_1-\gamma_2}{\xi_L k_B T} - ln\frac{\xi_L}{\xi_0}\right)}}. \tag{6}$$

The maximum radius R_{max} of clusters that can enter the cell is limited by the number of available membrane receptors. Once the average concentration of free receptors outside the contact region drops to ξ_+, then the receptors (free and bound) reach chemical equilibrium and there is no further wrapping. This gives:

$$\pi L^2\xi_0 = 4\pi\ R_{max}^2\xi_L + (\pi L^2 - 4\pi R_{max}^2)\xi_+, \tag{7}$$

Thus, the critical radius can be estimated by combining the equation (Eq. (7)) for conservation of receptors on the membrane of characteristic size L with Eq. (5).

A simple estimate for the wrapping time can be obtained via the characteristic time of diffusion of receptors from the region of size $l{\sim}R\sqrt{\xi_L/\xi_0}$ that are needed to completely cover the cluster of nanoparticles. Hence, the wrapping time is given by:

$$t_w{\sim}\frac{l^2}{D}{\sim}\frac{R^2}{D}\frac{\xi_L}{\xi_0}, \tag{8}$$

where D is the diffusion constant of free membrane receptors. More accurate results take into account the detailed kinetics of the wrapping process, as described in Ref. [70].

3.3. Entry of clusters into normal breast cells and breast cancer cells

As in Ref. [30], the value of $\gamma_1 - \gamma_2$ in the free energy expression (presented in Eq. (3)) was estimated to be the surface energy difference between water on LHRH-MNPs surface and glycerol on LHRH-MNPs surface. Contact angle measurements were conducted for the two combinations and Young's equation was used to predict the new additional term, $(\gamma_1 - \gamma_2)/\xi_L$, which is on the order of $1.28k_BT$.

Since there are at least 120 amine groups (Ocean NanoTech, LLC., Private Communication, 2016) on the surface of the nanoparticles, the total number of LHRH ligands is expected to be on the same magnitude after conjugation. As the average hydrodynamic diameter of the particles is approximately 50 nm, the ligand density, ξ_L,is then estimated to be on the order of 15,000 μm^{-2}. The rest of parameters are adapted from Gao et al. [70]. Specifically, the receptor density, ξ_0, has a magnitude between 50 μm^{-2} and 500 μm^{-2}. Receptor-ligand binding energy, e_{RL}, is expected to be on the order of $15k_BT$ at $T = 300K$ [70]. The bending rigidity of biological cell membrane, B, has a value on the order of $20k_BT$ [70]. The diffusion coefficient of the receptors, D, is approximately 10^4 nm^2/s [70]. The length of the biological cell membrane, L, has a typical value of 10 μm [70]. For the listed parameters, we estimate that the minimum cluster size that can be encapsulated is $R_{min} = 14\ nm$ and the maximum cluster size is $R_{max} = 910\ nm$, where the intial receptor density is between 50 μm^{-2} and 500 μm^{-2}.

Furthermore, analytically, the cluster model predicts the wrapping times for different nanoclustersizes of clusters that are engulfed by a cell. The predictions are shown in Table 1. Here, we predict the wrapping time for cluster entry into cells under two conditions with different initial receptor densities in the membrane. The small ξ_0 has a value of 50 μm^{-2}, corresponding to approximately to 3900 receptors per cell, while the large ξ_0 has a magnitude of 500 μm^{-2}, corresponding to approximately 39,000 receptors per cell.

Although the exact number of specific LHRH binding sites per breast cancer/normal cell is not reported in the literature, the upper and lower bound values of ξ_0 are in the range that has been reported for binding sites between GnRH-Rs and MCF-7 breast cancer cells [77]. It is, therefore, reasonable to study the lower ξ_0 case as a model for normal

Table 1
Estimated wrapping time for different particle cluster sizes (radii) with initial receptor density of 50 μm^{-2} and 500 μm^{-2}.

Radius	50 nm	150 nm	250 nm	350 nm	450 nm	600 nm	750 nm	900 nm
$\xi_0 = 50$	9.1 min	1.4 h	3.7 h	7.4 h	12.2 h	21.7 h	1.4 days	2.1 days
$\xi_0 = 500$	33.3 s	5 min	13.9 min	27.2 min	44.9 min	1.3 h	2.1 h	3 h

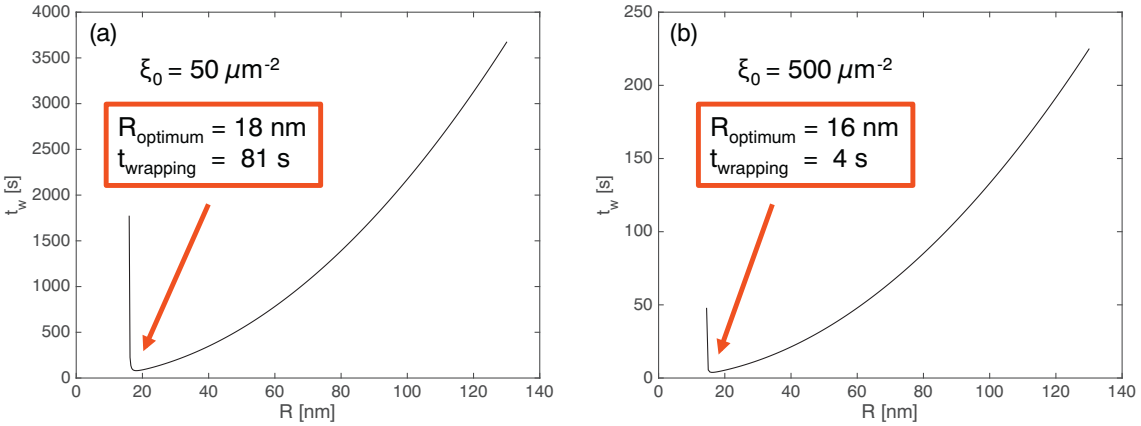

Fig. 4. The wrapping time, t_w, versus the radius, R, for an infinite cell membrane to take particle clusters with (a) initial receptor density of 50 μm^2, and (b) initial receptor density of 500 μm^2. The arrows are pointing to the minimum wrapping time, $t_{wrapping}$, and the corresponding optimum particle radius for encapsulation, $R_{optimum}$.

breast cells, while the large initial receptor density corresponds to breast cancer cell receptor distributions. The optimum cluster radius for $\xi_0 = 50\ \mu m^{-2}$ is obtained to be 18 nm and the corresponding wrapping time is estimated to be 81 s (Fig. 4a). Also, the optimum cluster radius for the cancer cell model with $\xi_0 = 500\ \mu m^{-2}$ is 16 nm, which is comparable to that of the normal cell model (Fig. 4b). However, the wrapping time of 4 s is twenty times less.

4. Results

4.1. Nanoparticle characterization

The magnetite nanoparticles that were used in this study have an Fe_3O_4 core with PEG coating. The surfaces of the MNPs have functional amine groups to enable the conjugation of LHRH peptides to these PEG-coated MNPs. The fluorescamine protein assay showed that there were at least 120 amine groups per particle (Ocean NanoTech, LLC., Private Communication, 2016).

4.1.1. Phase identification

Since magnetite and maghemite both have cubic structures with similar lattice parameters, traditional XRD cannot distinguish easily between these two types of iron oxide. Hence, Raman spectroscopy was used to determine the type of iron oxide that was used in this study. This is because Raman spectroscopy is sensitive to the electron configuration of cation oxidation states and the characteristic peaks can distinguish different iron oxides from each other. The following modes and peak assignments were observed for MNPs in the Raman spectrum shown in Fig. 5: ${T_{2g}}^1$ for 186 cm^{-1}, ${T_{2g}}^2$ for 482 cm^{-1}, and A_{1g} for 662 cm^{-1}. These three peaks confirmed that the MNPs were magnetite. They are also in agreement with those that have been reported in the literature [78–80]. Furthermore, it is interesting to note that the Raman spectrum reveals the presence of the PEG coating, as A_1 for 862 cm^{-1}, and amine surface groups, where 3161 cm^{-1} represents the N—H symmetric stretching and 3232 cm^{-1} correspond to N—H asymmetric stretching (Fig. 5).

4.1.2. Structure

The TEM images revealed that the PEG-coated MNPs had spherical shapes, with an average core diameter of around 30 nm (Fig. 6a). A representative high resolution TEM image of MNPs is shown in Fig. 6b. It also illustrates that, due to the surface PEG coatings, the MNPs are separated from each other, and no aggregation is observed. The selected area diffraction pattern (SAD) confirmed that the particles were magnetite, since the ring pattern/assignments are in agreement with those reported for magnetite in the literature [81–84] (Fig. 6c). Finally, the energy dispersive X-ray spectroscopy (EDS), performed in TEM, also confirmed the presence of both Fe and O (Fig. 6d).

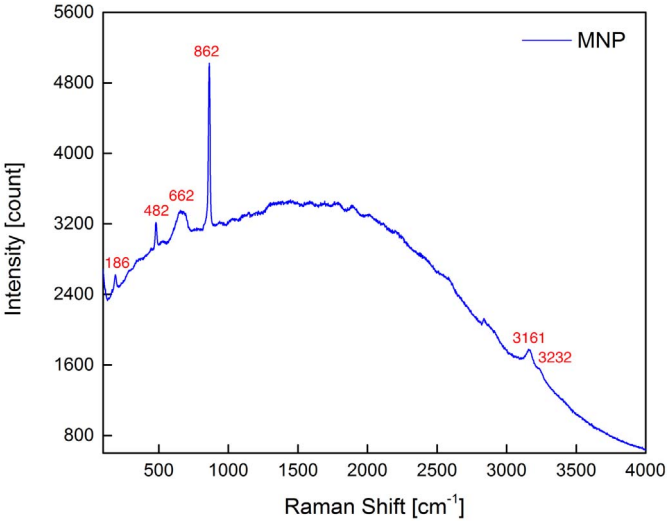

Fig. 5. Raman spectrum of MNPs.

4.1.3. Conjugation

The FTIR spectra of: (a) MNPs; (b) glutaraldehyde-activated MNP, and (c) LHRH-conjugated MNPs are presented in Fig. 7. All of the spectra exhibited peaks that were characteristic of PEG-coated iron oxide [66,69]. These included: the Fe—O bond at 590 cm^{-1}, and the —OH group found on the particle surface at 3300 cm^{-1}. The peaks at 1010, 1076, 1107 and 1153 cm^{-1}, correspond to the C-O-C and C—H bonds in PEG.

The FTIR spectrum of the PEG-coated MNPs exhibited characteristics of amine-terminated PEG with methylene signature peaks at 2935 and 2864 cm^{-1}. FTIR also confirmed the presence of the surface NH_2 groups, which corresponds to the peak at 1550 cm^{-1}. This vanished from the spectrum for both glutaraldehyde activated MNPs and LHRH-MNPs, as the surface amine groups react with carbonyl groups (at 1724 cm^{-1}) in glutaraldehyde.

During the peptide conjugation process, the amine groups in the peptides react with the remaining carbonyl group in glutaraldehyde. As a result, the carbonyl group that is present in (b) disappears in spectrum (c), while the relative intensity of C=N increases. These are located at 1203, 1346 and 1643 cm^{-1}, respectively. Hence, the FTIR spectra showed that the conjugation process was successful in forming the desired chemical bonds.

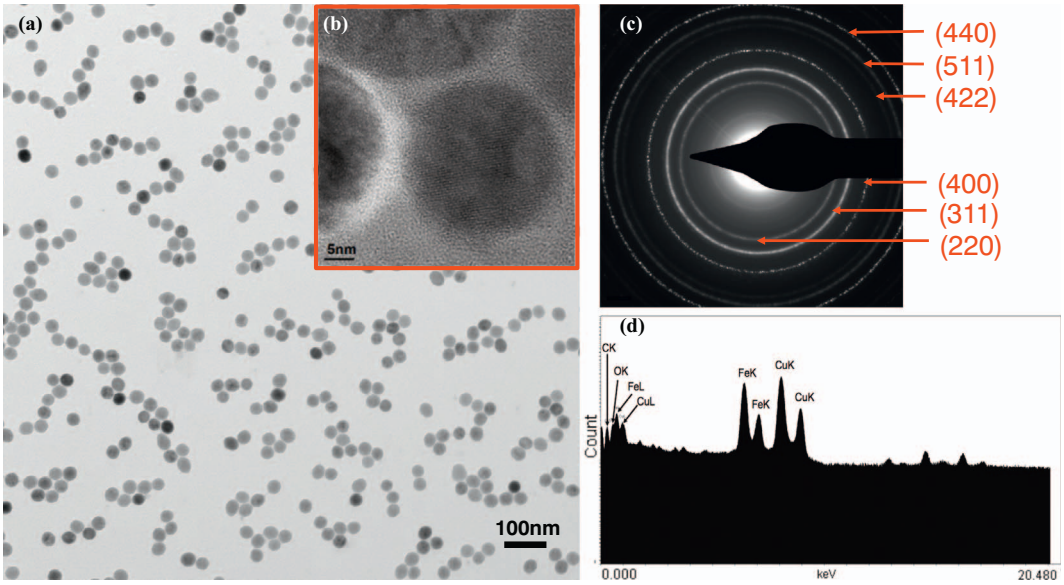

Fig. 6. (a) TEM micrograph of MNPs; (b) HRTEM image of MNPs; (c) Diffraction pattern of MNPs; and (d) EDS spectrum of MNPs.

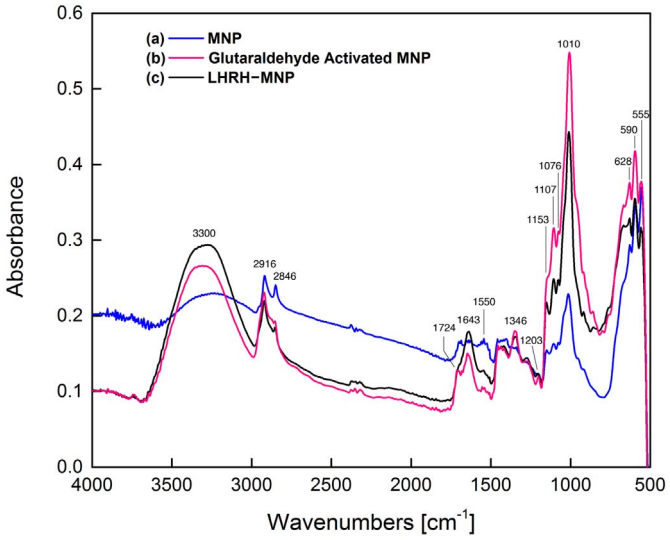

Fig. 7. FTIR spectra of (a) MNPs; (b) glutaraldehyde activated MNPs; and (c) LHRH conjugated MNPs.

4.1.4. Nanoparticle size distributions

The size distributions of the nanoparticles that were measured before and after peptide conjugation are presented in Table 2. Specifically, MNP has core diameter of 31.9 ± 2.4 nm and hydrodynamic diameter of 58.1 ± 17.2 nm. The core diameter and hydrodynamic diameter for LHRH-MNPs are 32.1 ± 2.1 nm and 59.3 ± 19.1 nm, respectively. These were obtained by calculating: core diameters from TEM micrographs (Fig. 8a) and hydrodynamic diameters from Dynamic Light Scattering (DLS) (Fig. 8b). The polydispersity index (PDI) values measured for MNPs and LHRH-MNP dispersions in DI water (hydrodynamic diameter) were both < 0.1. The values were obtained by DLS device according to the ISO standard document 13,321:1996 E [85] and ISO 22412:2008 [86]. PDI values indicates the width of the overall size distribution, with a value ranging between 0 (monodisperse) and 1 (polydisperse) [87–89]. Here, low PDI numbers (0.07 for MNPs and 0.09 for LHRH-MNPs) indicate that the nanoparticles used in this study have good monodispersity.

Table 2
Colloidal properties of iron oxide nanoparticles before and after LHRH conjugation.

Sample	Core diameter [nm]	Hydrodynamic diameter [nm]	Polydispersity index in DI water	Zeta potential [mV]
MNP	31.9 ± 2.4	58.1 ± 17.2	0.07	2.9 ± 0.3
LHRH-MNP	32.1 ± 2.1	59.3 ± 19.1	0.09	4.9 ± 0.6

4.1.5. Surface charge

Table 2 summarizes the ζ-potentials obtained for MNPs (2.9 ± 0.3 mV) and LHRH-MNPs (4.9 ± 0.6 mV) in DI water. While lower absolute value of the ζ-potential indicates the colloidal instability, which could lead to aggregation. The particles were well dispersed in water for > 6 months, with no flocculates or precipitates being observed during this period. Hence, their application will not be impaired during this period of time.

4.2. Nanoparticle entry into cells

4.2.1. Cellular uptake characterization by TIRF and confocal microscopes

The internalization of nanoparticles into the cells at different incubation times was characterized for the following particle/cells combinations: MNPs with MDA-MB-231 TNBC cells, LHRH-MNPs with MDA-MB-231 TNBC cells, and LHRH-MNPs with MCF-10A normal breast cells, as shown in Fig. 9.

After 5 min of incubation, LHRH-MNP particles were greatly attracted to MDA-MB-231 breast cancer cells, forming clusters at the cell membranes (Fig. 9g). However, large clusters did not form with MNPs or with LHRH-MNPs and MCF-10A normal breast cells (Fig. 9b and l).

MNPs started to enter into the cancer cells and small nano-clusters were observed in the cytoplasms of the cells within 5 min (Fig. 9b). These clusters became more obvious after 30 min and 1 h, as shown in Fig. 9c and d respectively. After 3 h of uptake, small MNP clusters were observed in the cytoplasm and the nuclei (Fig. 9e).

For the internalization of LHRH-MNPs into normal breast cells, no detectable nanoparticle/cell interactions were observed after 5 min (Fig. 9l). However, after 1 h, LHRH-MNP clusters were observed on the cell membranes. These LHRH-MNP clusters were much smaller diameter than the LHRH-MNPs in the cancer cells (Fig. 9h, i and j). The LHRH-MNP clusters entered into the normal breast cells and were observed inside of the cytoplasm of these cells after 1 h. Larger clusters were internalized into normal cells after 3 h (Fig. 9o).

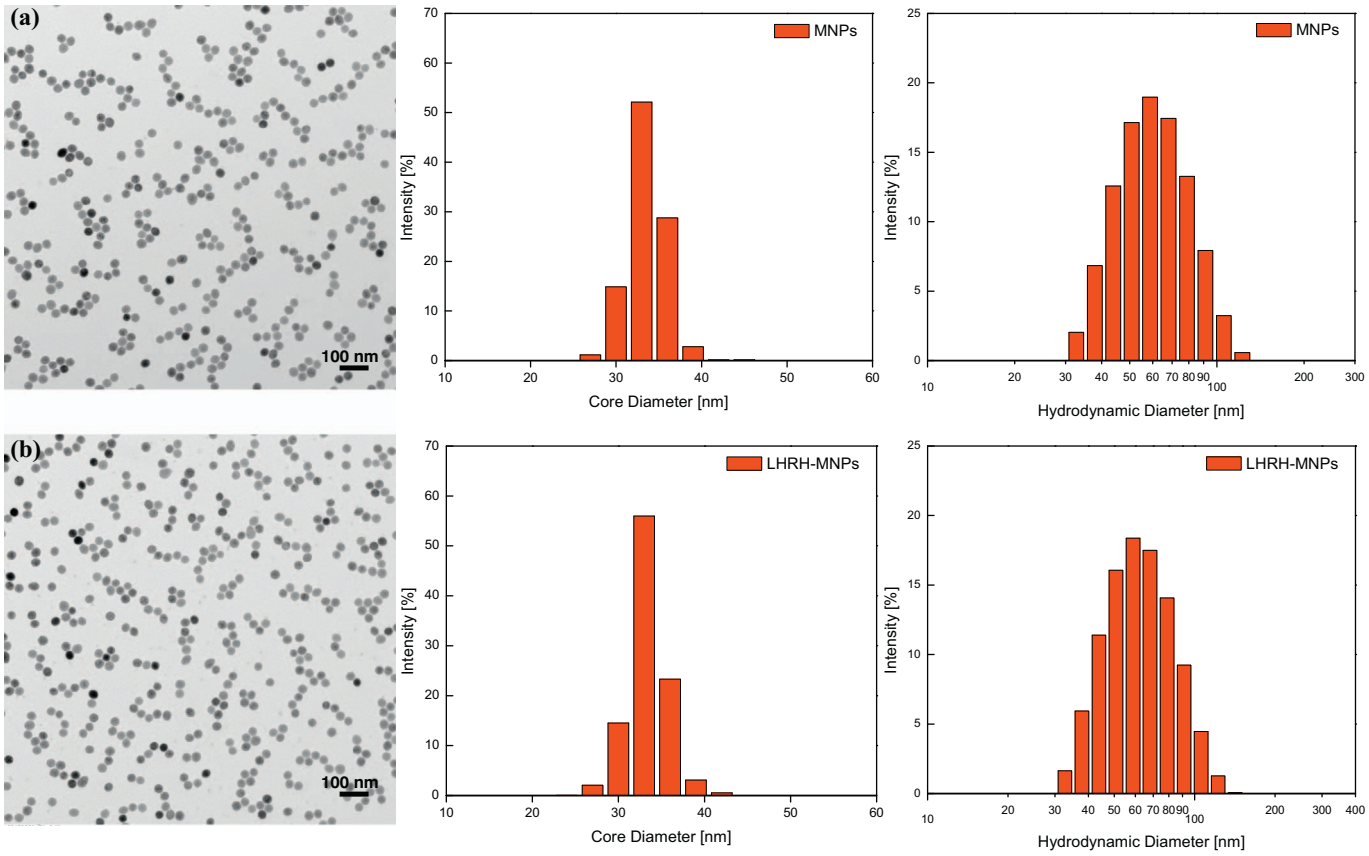

Fig. 8. TEM images, core diameters and hydrodynamic diameters of (a) MNPs in water; and (b) LHRH-MNPs in water.

The interactions between LHRH-MNPs and breast cancer cells became more obvious with increasing time. After 1 h, LHRH-MNPs had already entered into the cancer cells and were present in the cytoplasm outside the nuclei (Fig. 9i). Furthermore, some LHRH-MNP particles were observed in the nuclei after 3 h (Fig. 9h). It is also interesting to note that at 5 min, the LHRH-MNP cluster sizes were on the order of about 10 μm on the surface of breast cancer cells (Fig. 10a). However, during the later stages, the clusters that were present inside of the cells had significantly smaller sizes of approximately 3 μm (Fig. 10b).

The internalization of LHRH-MNPs into breast cancer cells was also examined using confocal fluorescence microscopy. Fluorescein staining (FITC) revealed the presence of LHRH ligands (green fluorescence) on the surfaces of LHRH-MNP clusters (Fig. 11b and c). For 1-h incubation (Fig. 11a, b and c), clusters with different average radii, ranging from 250 nm to 900 nm, were observed inside the cytoplasms and the nuclei of the breast cancer cells. After 3-h of uptake, more clusters with larger sizes were observed in the breast cancer cells.

Focusing on the region highlighted in yellow, a few LHRH-MNP clusters, identified with arrows, were found inside of the nuclei after 3 h of incubation. Clusters were also observed on the cell membrane. They were observed to enter the cells via receptor-mediated endocytosis (Fig. 11e and f). The LHRH-conjugated magnetite particles that entered the breast cancer cells after 3 h of incubation had diameters in the range between 400 nm and 1.5 μm.

The positions of the internalized nanoparticle clusters in MDA-MB-231 cells were also confirmed using confocal fluorescence microscopy with a step size of 100 nm in the z-direction. The slices extracted via 3D imaging of cells (at different z-heights) are presented in Fig. 12. Also, the particles in Fig. 12d are not observed in Fig. 12a, b and e, indicating these clusters were internalized inside of the cells. These observations again suggest that nanoparticles entered into the breast cancer cells via receptor-mediated endocytosis.

4.2.2. *Cluster size distribution and cellular uptake efficacy*

The fully engulfed cluster size distributions in three types of nanoparticle/cell interactions per incubation times are reported in bar charts in Fig. 13a, b and c. Fig. 13a shows the results of MNP cluster size distribution in MDA-MB-231 breast cancer cells at incubation times of 5 min, 30 min, 1 h and 3 h. The majority of the clusters have diameters < 2 μm. Specifically, at 5-min incubation time, up to 79.4% of clusters fall into the size range between 0.5 μm to 1 μm. After 30 min cellular uptake, the major peak shifts to range between 1.5 μm and 2 μm (~57.1%). Larger clusters, with diameters over 2 μm, were observed more frequently with increasing incubation times. For instance, clusters up to 4 μm diameter (~1%) were present after 3 h. The difference between the overall cluster size distributions at various incubation times is statistically significant ($p < .001$). Similar trends are also observed in the cases of LHRH-MNPs/breast cancer cells ($p < .001$) and LHRH-MNPs/normal breast cells ($p < .001$).

To quantify the efficacy of cellular uptake, the cluster uptake percentage was estimate from the ratio of the total encapsulated cluster area to the total cell area in the field of view. The results are presented in Fig. 13d. During the interaction between MNPs and breast cancer cells, there is an increase in uptake efficacy from 0.06% (at 5 min) to 0.79% (at 3 h). For the efficacy in LHRH-MNPs/breast cancer cells, the initial value at 5 min is 0.025%. This rises to 1.3% after 3 h, which is almost twice as much as that between MNPs and breast cancer cells. Lastly, in the cellular uptake of LHRH-MNPs into normal breast cells, there is a slight increase in efficacy initially from 5 min (0.025%) to 1 h (0.158%), but no notable changes afterwards. Overall, there is an acceptable level of statistical significance ($p = .057$) in the uptake efficacy between these three types of interactions.

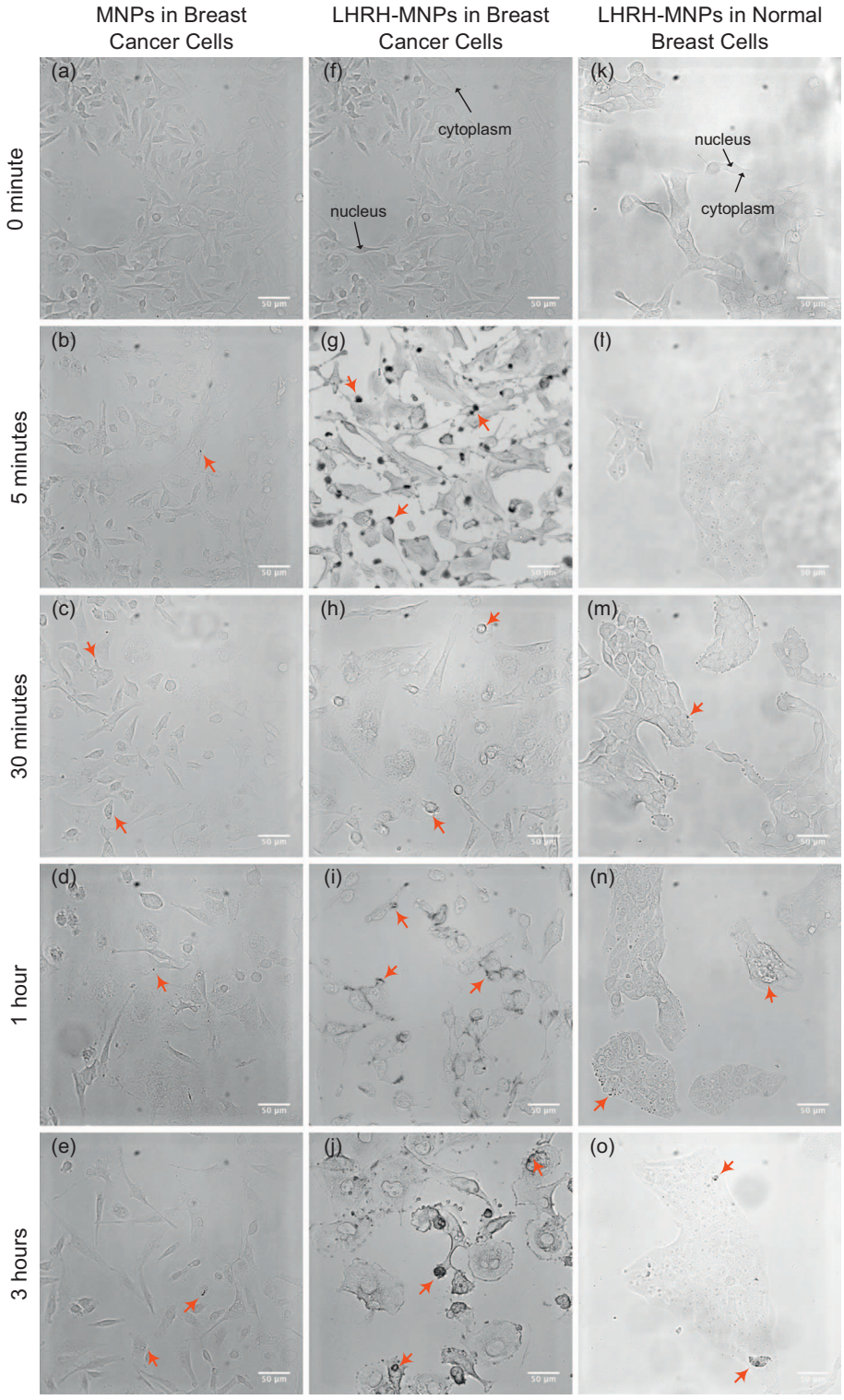

Fig. 9. Representative images of NP internalization into cells for three NP/cell combinations at 5 min, 30 min, 1 h and 3 h after incubation: MNPs/MDA-MB-231 breast cancer cells, LHRH-MNPs/MDA-MB-231 breast cancer cells and LHRH-MNPs/MCF-10A normal breast cells. (scale bars: 50 μm, red arrows pointing towards representative NP locations). (For interpretation of the references to color in this figure legend, the reader is referred to the web version of this article.)

5. Discussion

5.1. Nanoparticle characterization

The results presented in Table 2 show that the hydrodynamic diameters of LHRH-MNPs are greater than the core diameters obtained from the TEM images. This is because the DLS measures the hydrodynamic diameter (also known as intensity averaged particle diameter), which is a combination of the actual nanoparticle size and the surrounding solvent molecules. Furthermore, the organic layer (PEG) coating on the MNPs is transparent to electron beams in the TEM. It is also known that the thickness of the grafted PEG layer (on the nanoparticle surface) correlates with polymer conformation, which is bushy-like [60]. Hence, the hydrodynamic diameter is larger than the

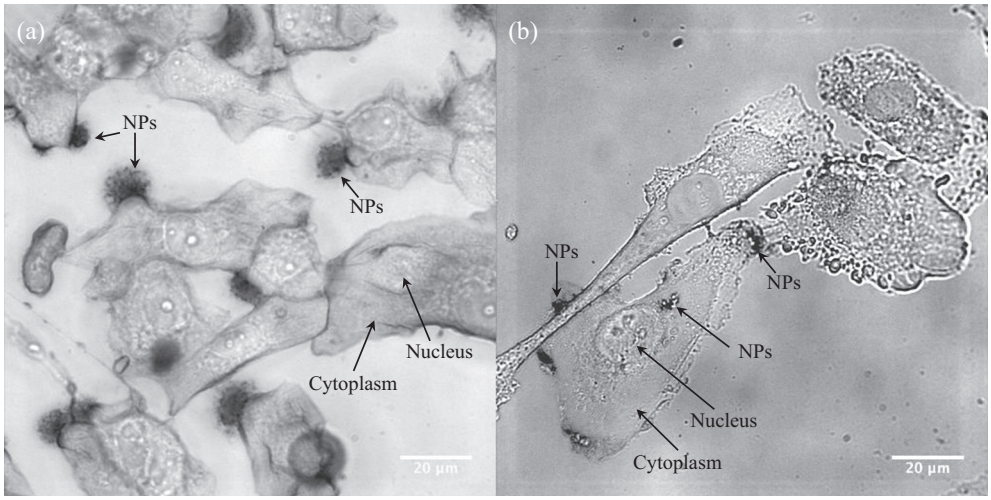

Fig. 10. LHRH-MNPs internalization into MDA-MB-231 breast cancer cells at 60× magnification for (a) 5 min incubation and (b) 3 h incubation. (Scale bars: 20 μm).

core diameter (Table 2).

The polydispersity index (PDI) serves as an important indicator for both nanoparticle stability and size uniformity. A greater PDI value (towards 1) corresponds to wider size distribution while a lower PDI value (towards 0) indicates the sample size range is narrower [89]. In our study, low PDI values were obtained (0.07 for MNPs and 0.09 for LHRH-MNPs), meaning that the particles have good monodispersity and stability. It is important to note that both the MNPs and LHRH-MNPs had narrow size distributions that suggest that minimal aggregation occurred during ligand exchange. This indicates that maximum possible number of ligands (~120 per particle) (Ocean NanoTech, LLC., Private Communication, 2016) has been attached to the nanoparticle surface and allows highest level of interaction with receptors. Aggregation among particles will reduce the effectiveness of ligand-conjugated carriers for specific targeting purpose.

The surface charges of nanoparticles also play an important role in

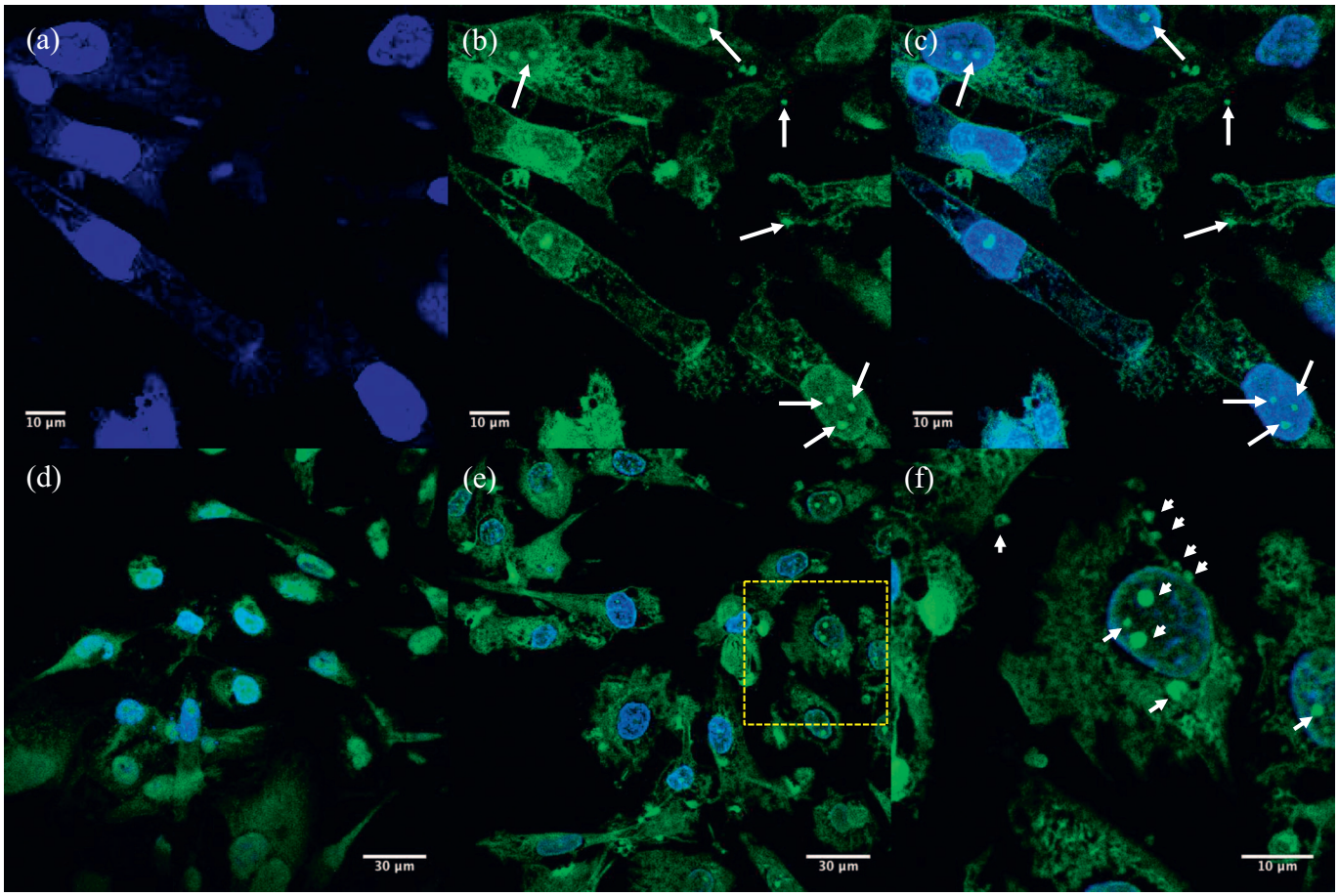

Fig. 11. Confocal fluorescence images: (a) DAPI (4′, 6-diamidino-2-phenylindole) for LHRH-MNPs incubated in MDA-MB-231 breast cancer cells for 1 h; (b) FITC (fluorescein isothiocyanate) for same cells; (c) combined DAPI and FITC with arrows pointing towards clusters; (d) MDA-MB-231 breast cancer cells (no particles); (e) LHRH-MNPs incubated into MDA-MB-231 breast cancer cells for 3 h; and (f) enlarged area for highlighted region in (e) with arrow pointing towards clusters.

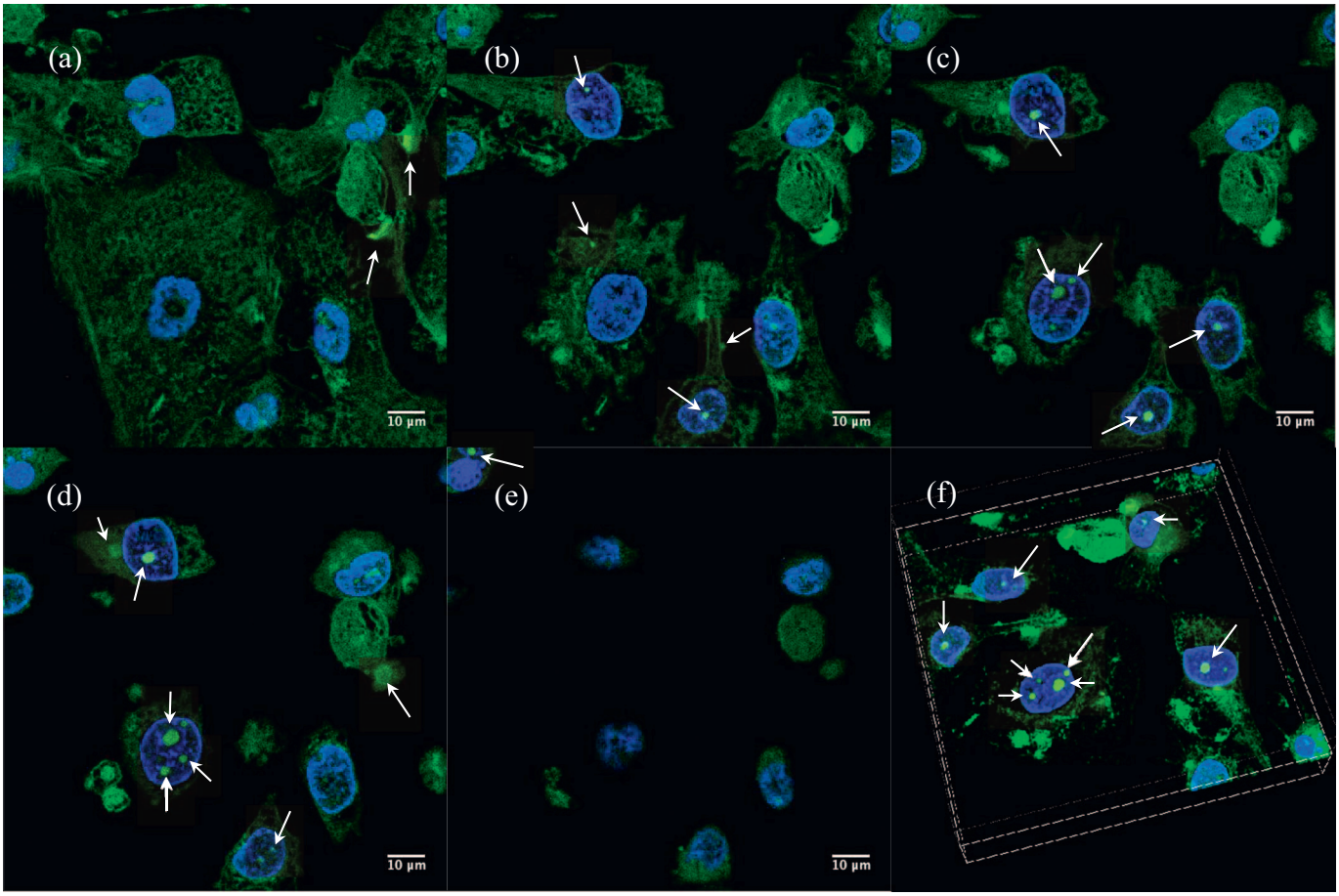

Fig. 12. 3D confocal fluorescence image of LHRH-MNPs incubated into MDA-MB-231 breast cancer cells for 3 h, with a) to e) being slices taken at different z height, from bottom to top, and f) being a partial 3D image that is sliced at certain z-height. Particles are exposed at various locations at different z heights.

the interactions with cell membranes [90,91]. Also, the stability of MNPs suspension can be referred from the absolute value of the ζ-potential [92]. It is clearly demonstrated that the absolute values of the ζ-potential for both MNPs and LHRH-MNPs are positive (Table 2). The positive surface charge is favorable for the interactions between the nanoparticles and biological cells, since the cell membrane is negatively charged [93].

5.2. Nanoparticle uptake by breast cells

The size distribution of nanoparticle clusters and their uptake efficacy into breast cells (both normal and cancerous) were presented in Section 4.2.2. The smallest detectable cluster sizes are limited due to the resolution of optical and fluorescence microscopes. Therefore, dispersed nanoparticle distribution was not reported while individual nanoparticle and cell interaction can be virtualized using TEM images [30]. Nevertheless, the experiments clearly demonstrated that the presence of LHRH ligands facilitate functionalized nanoparticles accumulation inside of breast cancer cells, which over express LHRH receptors on their surfaces [73]. Overall, the amount and sizes of clusters observed inside normal breast cells were significantly lower than in the cancer cells at comparable times.

Ligand-conjugated nanoparticles typically enter into the cells though receptor mediated endocytosis once they reach the target and bind to receptors [94,95]. The comparison in cellular uptake for different cell/nanoparticle pairs suggests that LHRH-MNPs preferentially enter into breast cancer cells through receptor-mediated pathways (Fig. 9). Leuschner et al. [43] reported LHRH receptor binding affinity and binding capacity values, which again emphasized that the endocytosis pathway of LHRH-MNPs entering into breast cancer cells is receptor-dependent. To clarify whether this process is clathrin dependent, sucrose and intracellular potassium depletion method can be used to further study the mechanism pathway [96]. However, this is beyond the scope of this paper.

Nanoparticles can also enter into cells through pathways that do not involve receptors, which happens in MNPs/breast cancer cells and LHRH-MNPs/normal breast cells. In such cases, the particles can be internalized by cells via receptor independent pathways, e.g. phagocytosis. While the results indicated that receptor-mediated process is more efficient in cellular uptake. There is also a chance that LHRH-MNPs can be engulfed into breast cancer cells via both receptor-mediate endocytosis and phagocytosis. The detailed pathways which are involved in this process, though, require further investigation.

5.3. Comparison of models and experiments

The modeling results suggest that the wrapping process between LHRH-MNPs and the breast cell is accelerated by the increased incidence of receptors on the membranes of cancerous cells. Hence, the wrapping process is overall quicker for breast cancer cells than for normal cells (Fig. 4), and Table 1 indicates that the wrapping time increases with increasing cluster sizes. For cluster radii that are over 600 nm, the model predicts that it takes over one day for the cluster to be wrapped into a normal cell. However, the overall wrapping times for nanoparticles engulfed into cancer cells is much less, indicating LHRH-MNPs are kinetically favorable for entry into breast cancer cells.

Therefore, we conclude that receptor-mediated endocytosis involves an interplay between thermodynamics and kinetics [30,70]. When the

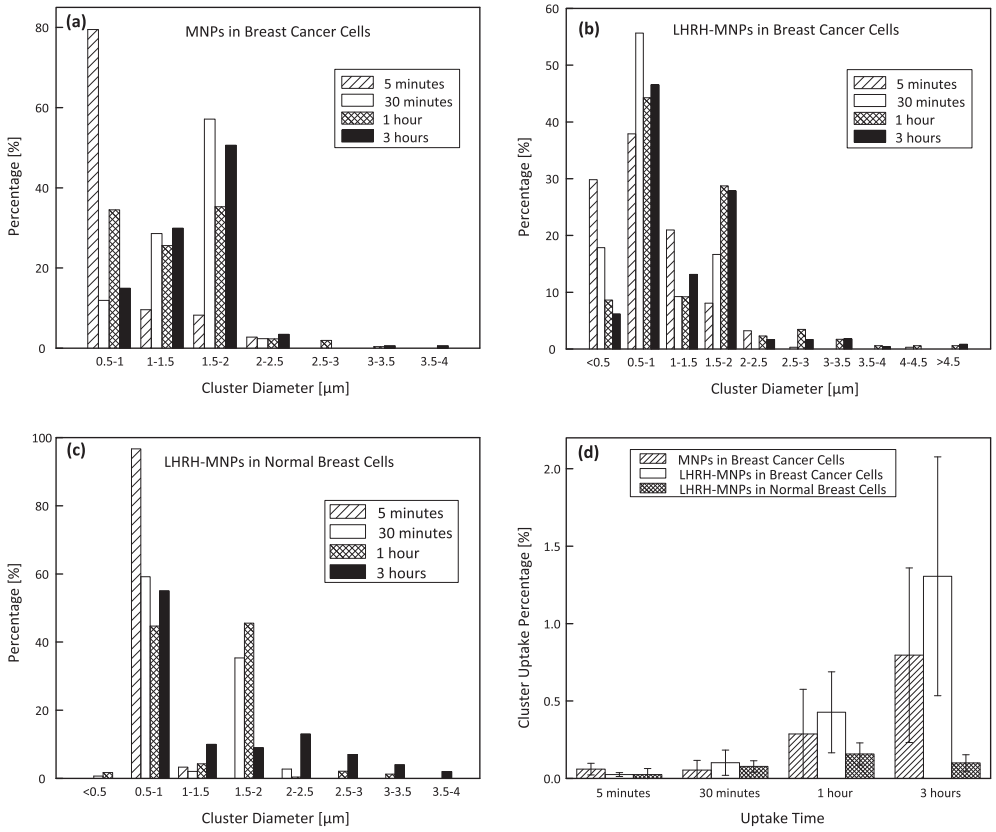

Fig. 13. Nanoparticle cluster size distribution at 5 min, 30 min, 1 h and 3 h for (a) MNPs/MDA-MB-231 breast cancer cells; (b) LHRH-MNPs/ MDA-MB-231 breast cancer cells and (c) LHRH-MNPs/MCF-10A normal breast cells. (d) The estimated uptake percentage (total cluster area over total cell area) between three NP/cell combinations at different uptake time.

particle size is too small, the process becomes thermodynamically unfavorable, because a binding free energy due to small number of ligand-receptor pairs cannot overcome the cost of bending energy of cell membrane. For small particles, they can enter into cells through other pathways other than receptor-mediated endocytosis, such as direct penetration [74,75,97]. On the contrary, for large clusters, the entry is very slow, because it takes much longer for the membrane receptors to diffuse towards the clusters. For large clusters, it is also possible for the cell membrane to not have enough receptors for the receptor-mediated endocytosis process to occur. In this scenario, large clusters may enter via a different pathway, e.g. phagocytosis. As a result, there exist an optimum diameter, (~32 nm), which minimizes the entry time (see Fig. 4) in the context of cellular uptake into breast cancer cells.

This prediction is consistent with the experimental observations discussed in Section 4.2. Fig. 10b shows that the internalized cluster sizes after 3 h of incubation are much smaller than the cluster sizes (approximately 10 μm in diameter) presented on the cell membrane at early stages (Fig. 10a). These large sized clusters outside of the cancer cells were formed probably due to interfacial energy between the nanoparticles. In addition, specific interactions between LHRH receptor and its ligand could attract the conjugated nanoparticles towards binding sites, leading to the formation of large clusters, which are engulfed afterwards. Particularly, a single nanoparticle may not have large enough area to interact with enough numbers of receptors to drive the membrane wrapping process. By contrast, a group of nanoparticles forming into cluster at cell membrane enables greater binding affinity to large numbers of receptors and hence promote cellular uptake. This is not to say clustering is always favored. For example, clustering of particles in the original colloidal solution not only reduce ligand density but also have a higher chance of being eliminated by immune system. Thus, the delivery efficacy is not optimized.

The above results suggest that, during receptor-mediated endocytosis, although the larger clusters are more energetically favorable to be encapsulated, the process is less kinetically favorable due to the slow diffusion of receptor transport on the cell membrane. Moreover, with these extra-large clusters, there is a higher chance that the cell membrane will not have enough receptors that can fully support the whole clusters to enter cells. Therefore, such extra-large clusters formed at initial stages were not observed inside of breast cancer cells after longer incubation times, while smaller sizes of particle clusters were detected.

Furthermore, both the cluster size and the wrapping time predictions are in good agreement with the experimental observations shown in Section 4.2. For instance, in confocal and TIRF images, LHRH-MNPs with average radii up to 900 nm are observed after 1 h of incubation with breast cancer cells (Fig. 9i and Fig. 11c), while clusters with average radii up to 1.5 μm are present after 3 h of uptake (Fig. 9j, Fig. 10b and Fig. 12). On the contrary, the uptake of LHRH-MNPs in normal breast cells were present in significantly lower quantities and smaller sizes (Fig. 9o). This observation suggests that there is a specific interaction between LHRH conjugated nanoparticles and breast cancer cells. Such receptor-ligand interaction explains the higher uptake of the functionalized particles into breast cancer cells.

Finally, it is important to note that the analytical models assume that the cell membrane is infinite. If we consider finite cell membranes, the wrapping times will be larger than those predicted for infinite cell membranes. Since for finite size cell membrane, when the particle radius exceeds $R_{max} = 910\ nm$, the wrapping process cannot be completed due to the lack of receptors [70]. While for infinite size membrane, there will always be receptors diffusing towards the binding area to internalize particles. We have also idealized the wrapping time to be the time between the onset of initial nanoparticle/cell membrane contact and the onset of full engulfment of the nanoparticles. However, under in-vivo conditions, the transport of the nanoparticles to the

tumor sites should also be considered in addition to the receptor-mediated endocytosis process explored in this paper. This is clearly beyond the scope of the current work.

6. Conclusion

The entry of LHRH conjugated PEG-coated magnetite nanoparticles into triple negative breast cancer cells and normal breast cells has been studied using both thermodynamics and kinetics models, as well as in-vitro experiments. The comparisons of the different nanoparticle/cell combinations suggest that LHRH-MNPs enter preferentially into breast cancer cells via receptor-mediated endocytosis pathway. The specific interactions between LHRH receptors and ligands results in significant LHRH-MNP uptake after 3 h of interactions with breast cancer cells. The cluster size distribution and uptake efficacy show that the entry of LHRH-MNPs into breast cancer cells depend on the highly efficient receptors. The thermodynamics cluster model predicts that the cells can take in nanoclusters with radii between 14 nm and 910 nm. Also, the kinetics model predicts that the wrapping time for full encapsulation of the nanoclusters into breast cancer cells is between 30 s and 3 h, for clusters with radii between 50 nm and 900 nm. These predictions are in good agreement with experimental observations. Thus, these results suggest that LHRH-MNPs can be used for the specific targeting of TNBC cells in breast cancer detection and treatment.

Disclosures

The authors declare that there are no conflicts of interest.

Acknowledgements

The authors are grateful to the Princeton University's Old School Fund, the Princeton University School of Engineering and Applied Science Fund, the World Bank African Centers of Excellence Program and Worcester Polytechnic Institute (WPI) for their financial support.

References

[1] R.L. Siegel, K.D. Miller, A. Jemal, Cancer statistics, 2016, CA Cancer J. Clin. 66 (1) (2016) 7–30.
[2] P. Kumar, R. Aggarwal, An overview of triple-negative breast cancer, Arch. Gynecol. Obstet. 293 (2) (2016) 247–269.
[3] G. Bianchini, J.M. Balko, I.A. Mayer, M.E. Sanders, L. Gianni, Triple-negative breast cancer: challenges and opportunities of a heterogeneous disease, Nat. Rev. Clin. Oncol. 13 (11) (2016) 674–690.
[4] M. De Laurentiis, D. Cianniello, R. Caputo, B. Stanzione, G. Arpino, S. Cinieri, V. Lorusso, S. De Placido, Treatment of triple negative breast cancer (TNBC): current options and future perspectives, Cancer Treat. Rev. 36 (2010) S80–S86.
[5] T. Ovcaricek, S.G. Frkovic, E. Matos, B. Mozina, S. Borstnar, Triple negative breast cancer - prognostic factors and survival, Radiol. Oncol. 45 (1) (2011) 46–52.
[6] H.A. Wahba, H.A. El-Hadaad, Current approaches in treatment of triple-negative breast cancer, Cancer Biol. Med. 12 (2) (2015) 106–116.
[7] D.A. Hill, N.K. Horick, C. Isaacs, S.M. Domchek, G.E. Tomlinson, J.T. Lowery, A.Y. Kinney, J.S. Berg, K.L. Edwards, P.G. Moorman, S.E. Plon, L.C. Strong, A. Ziogas, C.A. Griffin, C.H. Kasten, D.M. Finkelstein, Long-term risk of medical conditions associated with breast cancer treatment, Breast Cancer Res. Treat. 145 (1) (2014) 233–243.
[8] P. Broet, S.M. Scholl, A. de la Rochefordiere, A. Fourquet, T. Moreau, Y. De Rycke, B. Asselain, P. Pouillart, Short and long-term effects on survival in breast cancer patients treated by primary chemotherapy: an updated analysis of a randomized trial, Breast Cancer Res. Treat. 58 (2) (1999) 151–156.
[9] C.L. Shapiro, A. Recht, Drug therapy - side effects of adjuvant treatment of breast cancer, N. Engl. J. Med. 344 (26) (2001) 1997–2008.
[10] Z.B. Li, E.Y. Ye, David R. Lakshminarayanan, X.J. Loh, Recent advances of using hybrid nanocarriers in remotely controlled therapeutic delivery, Small 12 (35) (2016) 4782–4806.
[11] D. Peer, J.M. Karp, S. Hong, O.C. FaroKhzad, R. Margalit, R. Langer, Nanocarriers as an emerging platform for cancer therapy, Nat. Nanotechnol. 2 (12) (2007) 751–760.
[12] K. Huang, Q.Q. Dou, X.J. Loh, Nanomaterial mediated optogenetics: opportunities and challenges, RSC Adv. 6 (65) (2016) 60896–60906.
[13] L.J. Zhang, T.J. Webster, Nanotechnology and nanomaterials: promises for improved tissue regeneration, Nano Today 4 (1) (2009) 66–80.
[14] E. Ellis, K.Y. Zhang, Q.Y. Lin, E.Y. Ye, A. Poma, G. Battaglia, X.J. Loh, T.C. Lee, Biocompatible pH-responsive nanoparticles with a core-anchored multilayer shell of triblock copolymers for enhanced cancer therapy, J. Mater. Chem. B 5 (23) (2017) 4421–4425.
[15] E.Y. Ye, M.D. Regulacio, S.Y. Zhang, X.J. Loh, M.Y. Han, Anisotropically branched metal nanostructures, Chem. Soc. Rev. 44 (17) (2015) 6001–6017.
[16] E.Y. Ye, M.D. Regulacio, M.S. Bharathi, H. Pan, M. Lin, M. Bosman, K.Y. Win, H. Ramanarayan, S.Y. Zhang, X.J. Loh, Y.W. Zhang, M.Y. Han, An experimental and theoretical investigation of the anisotropic branching in gold nanocrosses, Nano 8 (1) (2016) 543–552.
[17] C.P. Teng, T.L. Zhou, E.Y. Ye, S.H. Liu, L.D. Koh, M. Low, X.J. Loh, K.Y. Win, L.H. Zhang, M.Y. Han, Effective targeted photothermal ablation of multidrug resistant bacteria and their biofilms with NIR-absorbing gold nanocrosses, Adv. Healthc. Mater. 5 (16) (2016) 2122–2130.
[18] R.A. Revia, M.Q. Zhang, Magnetite nanoparticles for cancer diagnosis, treatment, and treatment monitoring: recent advances, Mater. Today 19 (3) (2016) 157–168.
[19] A.K. Gupta, M. Gupta, Synthesis and surface engineering of iron oxide nanoparticles for biomedical applications, Biomaterials 26 (18) (2005) 3995–4021.
[20] H. Ittrich, K. Peldschus, N. Raabe, M. Kaul, G. Adam, Superparamagnetic iron oxide nanoparticles in biomedicine: applications and developments in diagnostics and therapy, Rofo-Fortschritte Auf Dem Gebiet Der Rontgenstrahlen Und Der Bildgebenden Verfahren 185 (12) (2013) 1149–1166.
[21] Q.Q. Dou, X.T. Fang, S. Jiang, P.L. Chee, T.C. Lee, X.J. Loh, Multi-functional fluorescent carbon dots with antibacterial and gene delivery properties, RSC Adv. 5 (58) (2015) 46817–46822.
[22] S.T. Yang, L. Cao, P.G.J. Luo, F.S. Lu, X. Wang, H.F. Wang, M.J. Meziani, Y.F. Liu, G. Qi, Y.P. Sun, Carbon dots for optical imaging in vivo, J. Am. Chem. Soc. 131 (32) (2009) 11308.
[23] J.W. Park, Liposome-based drug delivery in breast cancer treatment, Breast Cancer Res. 4 (3) (2002) 93–97.
[24] T.M. Allen, P.R. Cullis, Liposomal drug delivery systems: from concept to clinical applications, Adv. Drug Deliv. Rev. 65 (1) (2013) 36–48.
[25] B.M. Teo, D.J. Young, X.J. Loh, Magnetic anisotropic particles: toward remotely actuated applications, Part. Part. Syst. Charact. 33 (10) (2016) 709–728.
[26] W.Q. Lim, S.Z.F. Phua, H.V. Xu, S. Sreejith, Y.L. Zhao, Recent advances in multi-functional silica-based hybrid nanocarriers for bioimaging and cancer therapy, Nano 8 (25) (2016) 12510–12519.
[27] Z. Li, M. Kawashita, N. Araki, M. Mitsumori, M. Hiraoka, M. Doi, Magnetite nanoparticles with high heating efficiencies for application in the hyperthermia of cancer, materials science &amp, Mater Sci Eng C Mater Biol Appl 30 (7) (2010) 990–996.
[28] R.A. Revia, M. Zhang, Magnetite nanoparticles for cancer diagnosis, treatment, and treatment monitoring: recent advances, Mater. Today 19 (3) (2016) 157–168.
[29] H.S. Huang, J.F. Hainfeld, Intravenous magnetic nanoparticle cancer hyperthermia, Int. J. Nanomedicine 8 (2013) 2521–2532.
[30] J. Meng, J. Fan, G. Galiana, R.T. Branca, P.L. Clasen, S. Ma, J. Zhou, C. Leuschner, C.S.S.R. Kumar, J. Hormes, T. Otiti, A.C. Beye, M.P. Harmer, C.J. Kiely, W. Warren, M.P. Haataja, W.O. Soboyejo, LHRH-functionalized superparamagnetic iron oxide nanoparticles for breast cancer targeting and contrast enhancement in MRI, Mater. Sci. Eng. C Biomim. Supramol. Syst. 29 (4) (2009) 1467–1479.
[31] L. Xiao, J. Li, D.F. Brougham, E.K. Fox, N. Feliu, A. Bushmelev, A. Schmidt, N. Mertens, F. Kiessling, M. Valldor, B. Fadeel, S. Mathur, Water-soluble superparamagnetic magnetite nanoparticles with biocompatible coating for enhanced magnetic resonance imaging, ACS Nano 5 (8) (2011) 6315–6324.
[32] Z.R. Stephen, F.M. Kievit, M. Zhang, Magnetite nanoparticles for medical MR imaging, Mater. Today 14 (7–8) (2011) 330–338.
[33] Z. Zhao, D. Huang, Z. Yin, X. Chi, X. Wang, J. Gao, Magnetite nanoparticles as smart carriers to manipulate the cytotoxicity of anticancer drugs: magnetic control and pH-responsive release, J. Mater. Chem. 22 (31) (2012) 15717–15725.
[34] R. Jurgons, C. Seliger, A. Hilpert, L. Trahms, S. Odenbach, C. Alexiou, Drug loaded magnetic nanoparticles for cancer therapy, J. Phys. Condens. Matter 18 (38) (2006) S2893–S2902.
[35] A.K. Gupta, S. Wells, Surface-modified superparamagnetic nanoparticles for drug delivery: preparation, characterization, and cytotoxicity studies, IEEE Trans. Nanobiosci. 3 (1) (2004) 66–73.
[36] D. Kami, S. Takeda, Y. Itakura, S. Gojo, M. Watanabe, M. Toyoda, Application of magnetic nanoparticles to gene delivery, Int. J. Mol. Sci. 12 (6) (2011) 3705–3722.
[37] S.C. McBain, H.H.P. Yiu, J. Dobson, Magnetic nanoparticles for gene and drug delivery, Int. J. Nanomedicine 3 (2) (2008) 169–180.
[38] J. Dobson, Gene therapy progress and prospects: magnetic nanoparticle-based gene delivery, Gene Ther. 13 (4) (2006) 283–287.
[39] C.W. Kwok, O. Treeck, S. Buchholz, S. Seitz, O. Ortmann, J.B. Engel, Receptors for luteinizing hormone-releasing hormone (GnRH) as therapeutic targets in triple negative breast cancers (TNBC), Target. Oncol. 10 (3) (2015) 365–373.
[40] S. Seitz, S. Buchholz, A.V. Schally, F. Weber, M. Klinkhammer-Schalke, E.C. Inwald, R. Perez, F.G. Rick, L. Szalontay, F. Hohla, S. Segerer, C.W. Kwok, O. Ortmann, J.B. Engel, Triple negative breast cancers express receptors for LHRH and are potential therapeutic targets for cytotoxic LHRH-analogs, AEZS 108 and AEZS 125, BMC Cancer 14 (2014).
[41] M. Fekete, J.L. Wittliff, A.V. Schally, Characteristics and distribution of receptors for D-TRP6-luteinizing hormone-releasing hormone, somatostatin, epidermal growth-factor, and sex steroids in 500 biopsy samples of human-breast cancer, J. Clin. Lab. Anal. 3 (3) (1989) 137–147.
[42] C. Fost, F. Duwe, M. Hellriegel, S. Schweyer, G. Emons, C. Grundker, Targeted chemotherapy for triple-negative breast cancers via LHRH receptor, Oncol. Rep. 25 (5) (2011) 1481–1487.
[43] C. Leuschner, C.S.S.R. Kumar, W. Hansel, W. Soboyejo, J. Zhou, J. Hormes, LHRH-conjugated magnetic iron oxide nanoparticles for detection of breast cancer

metastases, Breast Cancer Res. Treat. 99 (2) (2006) 163–176.
[44] J. Meng, E. Paetzell, A. Bogorad, W.O. Soboyejo, Adhesion between peptides/antibodies and breast cancer cells, J. Appl. Phys. 107 (11) (2010).
[45] J.D. Obayemi, S. Dozie-Nwachukwu, Y. Danyuo, O.S. Odusanya, N. Anuku, K. Malatesta, W.O. Soboyejo, Biosynthesis and the conjugation of magnetite nanoparticles with luteinizing hormone releasing hormone (LHRH), Mater Sci Eng C Mater Biol Appl 46 (2015) 482–496.
[46] K.L. Shannon, R.T. Branca, G. Galiana, S. Cenzano, L.S. Bouchard, W. Soboyejo, W.S. Warren, Simultaneous acquisition of multiple orders of intermolecular multiple-quantum coherence images in vivo, Magn. Reson. Imaging 22 (10) (2004) 1407–1412.
[47] B. Issa, I.M. Obaidat, B.A. Albiss, Y. Haik, Magnetic nanoparticles: surface effects and properties related to biomedicine applications, Int. J. Mol. Sci. 14 (11) (2013) 21266–21305.
[48] W. Wu, Q. He, C. Jiang, Magnetic iron oxide nanoparticles: synthesis and surface functionalization strategies, Nanoscale Res. Lett. 3 (11) (2008) 397–415.
[49] W. Wu, Z. Wu, T. Yu, C. Jiang, W.-S. Kim, Recent progress on magnetic iron oxide nanoparticles: synthesis, surface functional strategies and biomedical applications, Sci. Technol. Adv. Mater. 16 (2) (2015).
[50] T. Peik-See, A. Pandikumar, L.H. Ngee, M. Huang Nay, C.C. Hua, Magnetically separable reduced graphene oxide/iron oxide nanocomposite materials for environmental remediation, Cat. Sci. Technol. 4 (12) (2014) 4396–4405.
[51] J.J. Gooding, Peptide-modified electrodes for detecting metal ions, Electrochem. Sens. Anal. 49 (2007) 189–210.
[52] C. Corot, P. Robert, J.-M. Idee, M. Port, Recent advances in iron oxide nanocrystal technology for medical imaging, Adv. Drug Deliv. Rev. 58 (14) (2006) 1471–1504.
[53] H. Yue, W. Wei, Z. Yue, P. Lv, L. Wang, G. Ma, Z. Su, Particle size affects the cellular response in macrophages, Eur. J. Pharm. Sci. 41 (5) (2010) 650–657.
[54] M. Longmire, P.L. Choyke, H. Kobayashi, Clearance properties of nano-sized particles and molecules as imaging agents: considerations and caveats, Nanomedicine 3 (5) (2008) 703–717.
[55] N. Doshi, S. Mitragotri, Macrophages recognize size and shape of their targets, PLoS One 5 (3) (2010).
[56] M. Farina, D.S. Avila, J.B. Teixeira da Rocha, M. Aschner, Metals, oxidative stress and neurodegeneration: a focus on iron, manganese and mercury, Neurochem. Int. 62 (5) (2013) 575–594.
[57] C.G. Fraga, Relevance, essentiality and toxicity of trace elements in human health, Mol. Asp. Med. 26 (4–5) (2005) 235–244.
[58] H.C. Guo, E.Y. Ye, Z.B. Li, M.Y. Han, X.J. Loh, Recent progress of atomic layer deposition on polymeric materials, Mater Sci Eng C Mater Biol Appl 70 (2017) 1182–1191.
[59] W.G. Kreyling, A.M. Abdelmonem, Z. Ali, F. Alves, M. Geiser, N. Haberl, R. Hartmann, S. Hirn, D.J. de Aberasturi, K. Kantner, G. Khadem-Saba, J.M. Montenegro, J. Rejman, T. Rojo, I.R. de Larramendi, R. Ufartes, A. Wenk, W.J. Parak, In vivo integrity of polymer-coated gold nanoparticles, Nat. Nanotechnol. 10 (7) (2015) 619.
[60] J.V. Jokerst, T. Lobovkina, R.N. Zare, S.S. Gambhir, Nanoparticle PEGylation for imaging and therapy, Nanomedicine 6 (4) (2011) 715–728.
[61] B. Pelaz, P. del Pino, P. Maffre, R. Hartmann, M. Gallego, S. Rivera-Fernandez, J.M. de la Fuente, G.U. Nienhaus, W.J. Parak, Surface functionalization of nanoparticles with polyethylene glycol: effects on protein adsorption and cellular uptake, ACS Nano 9 (7) (2015) 6996–7008.
[62] U.S. Patil, S. Adireddy, A. Jaiswal, S. Mandava, B.R. Lee, D.B. Chrisey, In vitro/in vivo toxicity evaluation and quantification of iron oxide nanoparticles, Int. J. Mol. Sci. 16 (10) (2015) 24417–24450.
[63] V. Zavisova, M. Koneracka, J. Kovac, M. Kubovcikova, I. Antal, P. Kopcansky, M. Bednarikova, M. Muckova, The cytotoxicity of iron oxide nanoparticles with different modifications evaluated in vitro, J. Magn. Magn. Mater. 380 (2015) 85–89.
[64] A. Ruiz, Y. Hernandez, C. Cabal, E. Gonzalez, S. Veintemillas-Verdaguer, E. Martinez, M.P. Morales, Biodistribution and pharmacokinetics of uniform magnetite nanoparticles chemically modified with polyethylene glycol, Nano 5 (23) (2013) 11400–11408.
[65] Y. Zhang, C. Sun, N. Kohler, M.Q. Zhang, Self-assembled coatings on individual monodisperse magnetite nanoparticles for efficient intracellular uptake, Biomed. Microdevices 6 (1) (2004) 33–40.
[66] Y. Zhang, J. Zhang, Surface modification of monodisperse magnetite nanoparticles for improved intracellular uptake to breast cancer cells, J. Colloid Interface Sci. 283 (2) (2005) 352–357.
[67] J. Xie, C. Xu, N. Kohler, Y. Hou, S. Sun, Controlled PEGylation of monodisperse Fe_3O_4 nanoparticles for reduced non-specific uptake by macrophage cells, Adv. Mater. 19 (20) (2007) 3163.
[68] Y.J. Chen, J. Tao, F. Xiong, J.B. Zhu, N. Gu, K.K. Geng, Characterization and in vitro cellular uptake of PEG coated iron oxide nanoparticles as MRI contrast agent, Pharmazie 65 (7) (2010) 481–486.
[69] Y. Zhang, N. Kohler, M.Q. Zhang, Surface modification of superparamagnetic magnetite nanoparticles and their intracellular uptake, Biomaterials 23 (7) (2002) 1553–1561.
[70] H.J. Gao, W.D. Shi, L.B. Freund, Mechanics of receptor-mediated endocytosis, Proc. Natl. Acad. Sci. U. S. A. 102 (27) (2005) 9469–9474.
[71] F.M. Richards, J.R. Knowles, Glutaraldehyde as a protein cross-linking reagent, Journal of Molecular Biology 37 (1) (1968) 231 -&.
[72] K. Okuda, I. Urabe, Y. Yamada, H. Okada, Reaction of glutaraldehyde with amino and thiol compounds, J. Ferment. Bioeng. 71 (2) (1991) 100–105.
[73] J.D. Obayemi, J. Hu, V.O. Uzonwanne, O.S. Odusanya, K. Malatesta, N. Anuku, W.O. Soboyejo, Adhesion of ligand-conjugated biosynthesized magnetite nanoparticles to triple negative breast cancer cells, J. Mech. Behav. Biomed. Mater. 68 (2017) 276–286.
[74] N. Oh, J.-H. Park, Endocytosis and exocytosis of nanoparticles in mammalian cells, Int. J. Nanomedicine 9 (2014) 51–63.
[75] L. Shang, K. Nienhaus, G.U. Nienhaus, Engineered nanoparticles interacting with cells: size matters, Int. J. Nanotechnol. 12 (2014).
[76] E. Barrow, A.V. Nicola, J. Liu, Multiscale perspectives of virus entry via endocytosis, Virol. J. 10 (2013).
[77] A.R. Finch, L. Green, J.N. Hislop, E. Kelly, C.A. McArdle, Signaling and antiproliferative effects of type I and II gonadotropin-releasing hormone receptors in breast cancer cells, J. Clin. Endocrinol. Metab. 89 (4) (2004) 1823–1832.
[78] I. Chourpa, L. Douziech-Eyrolles, L. Ngaboni-Okassa, J.F. Fouquenet, S. Cohen-Jonathan, M. Souce, H. Marchais, P. Dubois, Molecular composition of iron oxide nanoparticles, precursors for magnetic drug targeting, as characterized by confocal Raman microspectroscopy, Analyst 130 (10) (2005) 1395–1403.
[79] O.N. Shebanova, P. Lazor, Raman study of magnetite (Fe_3O_4): laser-induced thermal effects and oxidation, J. Raman Spectrosc. 34 (11) (2003) 845–852.
[80] I. Chamritski, G. Burns, Infrared- and Raman-active phonons of magnetite, maghemite, and hematite: a computer simulation and spectroscopic study, J. Phys. Chem. B 109 (11) (2005) 4965–4968.
[81] K.C. Barick, M. Aslam, Y.-P. Lin, D. Bahadur, P.V. Prasad, V.P. Dravid, Novel and efficient MR active aqueous colloidal Fe_3O_4 nanoassemblies, J. Mater. Chem. 19 (38) (2009) 7023–7029.
[82] X. Shi, T.P. Thomas, L.A. Myc, A. Kotlyar, J.R. Baker Jr., Synthesis, characterization, and intracellular uptake of carboxyl-terminated poly(amidoamine) dendrimer-stabilized iron oxide nanoparticles, Phys. Chem. Chem. Phys. 9 (42) (2007) 5712–5720.
[83] X. Li, H. Si, J.Z. Niu, H. Shen, C. Zhou, H. Yuan, H. Wang, L. Ma, L.S. Li, Size-controlled syntheses and hydrophilic surface modification of Fe_3O_4, Ag, and Fe_3O_4/Ag heterodimer nanocrystals, Dalton Trans. 39 (45) (2010) 10984–10989.
[84] H.B. Xia, D.M. Cheng, C.Y. Xiao, H.S.O. Chan, Controlled synthesis of polyaniline nanostructures with junctions using in situ self-assembly of magnetic nanoparticles, J. Mater. Chem. 15 (38) (2005) 4161–4166.
[85] International Standard ISO13321, Methods for Determination of Particle Size Distribution Part 8: Photon Correlation Spectroscopy, International Standards Organization (ISO), 1996.
[86] International Standard ISO22412, Particle Size Analysis – Dynamic Light Scattering, International Organisation for Standardisation (ISO), 2008.
[87] P. Bihari, M. Vippola, S. Schultes, M. Praetner, A.G. Khandoga, C.A. Reichel, C. Coester, T. Tuomi, M. Rehberg, F. Krombach, Optimized dispersion of nanoparticles for biological in vitro and in vivo studies, Part. Fibre Toxicol. 5 (2008).
[88] J. Lim, S.P. Yeap, H.X. Che, S.C. Low, Characterization of magnetic nanoparticle by dynamic light scattering, Nanoscale Res. Lett. 8 (2013).
[89] R.C. Murdock, L. Braydich-Stolle, A.M. Schrand, J.J. Schlager, S.M. Hussain, Characterization of nanomaterial dispersion in solution prior to in vitro exposure using dynamic light scattering technique, Toxicol. Sci. 101 (2) (2008) 239–253.
[90] S. Honary, F. Zahir, Effect of zeta potential on the properties of nano-drug delivery systems - a review (part 1), Trop. J. Pharm. Res. 12 (2) (2013) 255–264.
[91] S. Honary, F. Zahir, Effect of zeta potential on the properties of nano-drug delivery systems - a review (part 2), Trop. J. Pharm. Res. 12 (2) (2013) 265–273.
[92] K.E. Sapsford, K.M. Tyner, B.J. Dair, J.R. Deschamps, I.L. Medintz, Analyzing nanomaterial bioconjugates: a review of current and emerging purification and characterization techniques, Anal. Chem. 83 (12) (2011) 4453–4488.
[93] N.M. Goldenberg, B.E. Steinberg, Surface charge: a key determinant of protein localization and function, Cancer Res. 70 (4) (2010) 1277–1280.
[94] S. Xu, B.Z. Olenyuk, C.T. Okamoto, S.F. Hamm-Alvarez, Targeting receptor-mediated endocytotic pathways with nanoparticles: rationale and advances, Adv. Drug Deliv. Rev. 65 (1) (2013) 121–138.
[95] L.M. Bareford, P.W. Swaan, Endocytic mechanisms for targeted drug delivery, Adv. Drug Deliv. Rev. 59 (8) (2007) 748–758.
[96] A.I. Ivanov, Pharmacological inhibition of endocytic pathways: is it specific enough to be useful? Methods Mol. Biol. 440 (2008) 15–33.
[97] D.A. Kuhn, D. Vanhecke, B. Michen, F. Blank, P. Gehr, A. Petri-Fink, B. Rothen-Rutishauser, Different endocytotic uptake mechanisms for nanoparticles in epithelial cells and macrophages, Beilstein J. Nanotechnol. 5 (2014) 1625–1636.